Experimental Characterization for Failure Behavior of Woven Modified Carbon/Carbon Composites Under Pin-Loading

Yanfeng Zhang
Harbin Institute of Technology
Zhengong Zhou (zhouzhg@126.com)
Harbin Institute of Technology
Zhiyong Tan
China Academy of Launch Vehicle Technology

Research Article

Keywords: modified carbon/carbon composites, mechanical response, failure mode, damage mechanism

Posted Date: November 12th, 2020

DOI: https://doi.org/10.21203/rs.3.rs-103484/v1

Abstract

An experimental approach of 5-harness satin woven silicon carbide modification carbon/carbon composites arranged in various geometrical configuration is presented in this paper. Seven types of samples divided into three groups were tested under pin-loading to examine the effects of width-to-hole diameter ratio (W/D), edge distance -to- hole diameter ratio (E/D) and hole diameter-to- thickness ratio (D/t) on the failure mode. To further enhance the understanding of failure propagation, damage mechanism was observed and assessed combining acoustic emission monitoring. From the experimental results and observations, it follows that the net tension and shearing out failure respectively switch to the bearing failure with the increasing ratio of W/D and E/D, while D/t hardly affect the failure mode. Major features of damage mechanism include matrix cracking, fiber buckling and pulling-out, interface debonding, delamination and fiber fracture corresponding to different acoustic emission signal ranges.

1. Introduction

With the development of current technology and productivity, composite materials are widely employed and gradually becoming a critical composing for structures in the aerospace field [1,2]. Most structures consist of assembly of individual components, and mechanical bolted joints are required to transfer loads between lots of parts to meet engineering applications. However, composites mechanical bolted joints are generally regarded as a source of weakness on account of brittleness, anisotropy and stress concentration attributed to drilling and bolting. Therefore, the failure analysis of composites joints has been experimentally and numerically performed [3-5]. Double-lap bolted joints eliminating the effect of load eccentricity can visually present failure modes, namely, net tension, shearing out, cleavage, and bearing. These failure modes refer to fiber bundle orientation, material properties, geometries, etc. Among these affecting factors, the fiber bundle orientation and material properties principally depend upon preparation process of materials, while the geometric dimension has larger designability.

Scholars have investigated the influence of geometry on strength of composite mechanical fastened joints. In early research, Collings [6] found the conversion from net tension failure to bearing failure is mainly influenced by the width-to- hole diameter ratio W/D and shearing out failure to bearing failure by the edge distance -to- hole diameter ratio E/D. Chang et al. [7] have developed a computer code which can be applied to joints involving fiber-reinforced laminates with different ply orientations, different material properties, and different configurations including hole sizes, hole positions and thickness. Aktas et al. [8] have investigated bearing strength and failure modes of a mechanically fastened carbon-epoxy composite plate of arbitrary orientation by experimental and numerical method. They found that full bearing strength is developed when E/ D and W/ D ratios are equal to or greater than 4, and the failure mode was shearing out when the above parameters were less than 4. Okutan [9] determined the failure of mechanically fastened E/glass–epoxy laminated composite joints. The results manifested that the failure mode change to bearing for [0/90/0]s and [90/0/90]s laminate with W/D and E/D became higher. Furthermore, for the [0/90/0]s laminate, failure mode is bearing when the E/D is larger than 3, and is

shear-out that is a weak type of failure for the small value of 3. A similar result was obtained for the critical W/D ratio. To the [90/0/90]s laminate, it was found that the critical E/D ratio was 4 for W/D = 2 and 3 and the critical E/D ratio was about 2 for W/D = 3 and 4.

In consideration of stability of composite materials damage process, bearing is caused by local compression and generally regarded as a progressive and preferable failure mode, while net tension, shear-out or cleavage are transient and catastrophic ones which should be averted as far as possible in connection structure design. Accordingly, relevant research concerned with bearing behavior of pin-loaded composites has been conducted. Camanho [10] et al. showed that bearing failure occurs by the process of local damage accumulation acting on the contact surface of the hole, where the damage mechanisms are fiber fracture and micro-buckling, matrix cracks, delamination at the loaded hole. Xiao [11] stated that bearing initial damage is triggered by kink-bands and delamination in 0° plies. Eriksson [12] reported that several important parameters including ply orientations and lateral constraint conditions have a marked effect on the bearing strength.

Compared to unidirectional composite laminates, less attention was paid to woven composites. Okutan [13] et al. examined the influence of W/D and E/D on the bearing strength of woven-glass-fiber reinforced epoxy laminated composites. The experimental results showed that the ultimate load capacity of the laminates with pin connections was increased by increasing W and E. However, increasing the E/D ratio beyond 2 and increasing the W/D ratio beyond 3 have an insignificant effect on the ultimate load capability of the connection. Karakuzu [14] et al. performed a study to deal with the bearing strength in woven laminated glass–vinylester composites and concluded that when W/D and E/D are increased, the bearing strength reaches higher values.

However, most previous research was limited to connecting structures of fiber reinforced composites including unidirectional laminated composites [6-12] and plain woven laminated composites [13,14]. Thereinto, unidirectional composites show excellent performance in a certain direction but weakness in others. In spite of stacking in different directions, delamination is apt to occur in the formed composites. For plain woven laminated composites, many interlacing points of warp and weft yarns lead to bending of fiber bundles, weakening excessively the material performance. Satin woven composites, especially the 5-harness satin (5HS) woven composites, are widespreadly applied in industry due to better resistance to impact and manufacturing flexibility compared to unidirectional composites. The warp and weft yarns are woven together with a certain regularity in 5HS. Since the float of yarns is longer and the interlacing points are fewer compared to plain woven architecture, the 5HS framework can still maintain a certain degree of fiber bundle straightness at the same time. On the other hand, reports of mechanical bolted joints almost referred to the materials with poor temperature tolerance (generally below 200℃), and rarely concerned with high-temperature-resistant materials. Carbon/carbon (C/C) composites are all-carbon materials with carbon fiber woven fabric as the reinforcement and resin carbon, asphalt carbon, or deposited carbon as matrix [15,16]. It is one of the few materials that can maintain high mechanical performance above 2000℃. Due to low density, low thermal expansion coefficient, high specific strength, high specific stiffness and excellent ablation and thermal shock resistance, C/C composites are key

thermal structural materials for aircraft design [17-19]. Whereas, the high temperature resistance of C/C composites is obtained mainly in a nonoxidizing atmosphere and materials oxidation begins at approximately 400℃ in the air, which results in a sharp attenuation of mechanical properties, limiting its in-depth application as temperature structural components. Silicon carbide matrix modification carbon/carbon composites (C/C-SiC) combining the excellent mechanical properties of carbon fiber and the high temperature properties of silicon carbide are being considered as one of the primary materials of launch vehicles. Hence, this paper presents an experimental investigation on the failure of 5HS woven C/C-SiC composites under pin-loading, which is the representative loaded mode in mechanical bolt joints, and focuses on achieving the following research objectives:

1. Provide the basic mechanical performance data of satin woven C/C-SiC composites including ultimate load, stiffness, for joints design and strength prediction, and evaluate the switching process of failure modes depending on the width-to-diameter ratio W/D, edge distance -to-diameter ratio E/D, diameter-to-thickness ratio t/D.
2. Combining acoustic emission (AE) monitoring, reveal the damage mechanisms by means of comparing the damage morphologies of several typical failure modes, and initially set up the matchup between AE signals of different levels and damage mechanisms.

2. Materials And Methods

The material preparation included forming of the carbon fiber woven preform, chemical vapor deposition (CVD) with pyrolytic carbon and silicon carbide matrix followed by densification cycles, and graphitization leading to C/C-SiC composites as show in Fig. 1(a). The preform architecture consisted of stacking 16 layers of 5HS woven fibers together. The fiber volume fraction of the finished composites was approximately 46%, and the resulting fabric micro-texture is shown in Fig. 1(b). In order to avoid the density inhomogeneity caused by traditional isothermal CVD process, the thermal gradient CVD was used in this research, which generated a temperature difference in the furnace forcing the deposited carbon to move through the preform.

width W, and a circular hole of diameter D, which was placed centrally with respect to the width and at an end distance E from the free edge, as shown in Fig. 2. All test pieces were machined by wire-electrode from a large plate with aforesaid material system. To consider influences of the geometric, the dimensions of plates designed respectively corresponded to three groups of experiments: variation of W/D, E/D and D/t. The first group was composed of varying W/D, while remaining E/D, D/t the same. The second group was composed of varying E/D, while remaining E/D, D/t the same. The third group was composed of varying D/t, while remaining W/D, E/D the same. Four samples were tested for each type with a geometric configuration and the seven types of samples as shown in Fig. 3, which were divided into three groups are detailed in Table 1. Before the tests, all samples were subjected to ultrasonic C-scan detection, which indicated specimens used no internal defects ascribed to the manufacturing. Compared to single-lap setup, double-lap setup in accordance with procedure A of ASTM Standard D5961 [20] was adopted to exclude secondary bending, as depicted in Fig. 2. The lower edge of the specimen was

clamped, and loading was applied on the pin in the warp bundles of the composites plate and symmetrical with respect to the centerline. In order to avoid compression damage, aluminum strengthening plate was pasted on the clamping area of test pieces. The high-strength steel alloy setup was much stiffer than the composites so that the deformation of the pin could be ignored. Experiment was performed in tension mode on a Zwick/Roell testing machine with 50 kN of maximum load capacity under displacement controlled at a rate of 0.1 mm/min to allow the time possible for observation of damage. Acoustic emission (AE) detection apparatus (Physical Acoustics Corporation PCI-2) was employed to monitor the local damage evolution and failure process of composites. The test set-up is shown in Fig. 4. To remove machine and ambient noises, the threshold for the AE was set to 45 dB. Corresponding cross-head load-displacement and AE events data were automatically recorded.

Table 1 Geometrical dimensions of test pieces.

Group number	Type number	W/D	E/D	D/t	Count
Group 1	Type A	2	3.5	1.2	4
	Type B	3.5			
	Type C	5			
Group 2	Type D	5	1.5	1.2	
	Type E		2.5		
	Type C		3.5		
Group 3	Type C	5	3.5	1.2	
	Type F			1.6	
	Type G			2	

3. Results And Discussion

3.1 Failure modes and global behavior

Detailed information of the failure patterns and typical load–displacement responses of three groups of specimens with different W/D, E/D and D/t obtained from experiments is illustrated in Fig. 5. For Group 1, distinct fracture surface roughly perpendicular to the loading direction can be observed for type A with the W/D of 2. Moreover, a hardly visible hole bearing deformation accompanying with flat surface around the hole illustrates almost no bearing failure occurred. Besides, no cracking is seen on the end face of the plate, which excludes shearing out and cleavage failure. Thus, net tension failure is diagnosed for type A. In respect of type B, except for the fracture surface along the width direction of the plate, an ovality resulting from a larger hole deformation and a small amount of matrix fragments and fractured fibers

near the edge of the hole are able to be observed, which indicates a combination of net tension and slight bearing failure occurred. As regards type C, massively local destructions adjacent to the hole and a serious hole deformation induced by bearing can be obviously observed. The local damage includes matrix crushing, transverse fibers bending, longitudinal fibers micro-buckling and a piece of material out-of-plane bulging. In addition, a fracture surface approximately along the center line of the plate and starting from the end face and extending into the plate can be found. It follows that remarkable bearing resulting in secondary cleavage is the final failure mode. For Group 2, representative shearing out failure mode characterized by evident two fracture surfaces roughly parallel the loading direction, materials pushed-out from the end face and a small deformation can be observed in type D. When E/D increases to 2.5 for type E, compared to type D, a smaller hole deformation occurred and a cleavage rather than shearing surface almost from the end face to the hole edge is apparent, which derives that cleavage led to the final failure. With the E/D increases to 3.5, the largest hole deformation and most severe local damage appeared for type C and, consequently, as mentioned above, full enough bearing failure happened. As to Group 3, hole deformations in the same extent and similar bearing failure modes leading to secondary cleavage can be found, which reveals D/t has little effect on the failure mode.

The load–displacement response of type A present a simple linear elastic shape signifying almost no damage occurred until the ultimate load. Then the load-bearing capacity dropped sharply, which manifests typical brittle failure characteristics. Except for type A, the curves for other types can be seemed as a three-phase variation as depicted on the curves of type C. Phase I: After initial contact leading to assembly clearance elimination accompanied by a short nonlinear form, the curves of all specimens are nearly linear until a knee point and no damage occurred. Similar stiffness can be obtained at this stage for all specimens since it was primarily dominated by the elastic hole deformation and dependent on the local bearing between the pin and hole contact surface, while hardly influenced by the geometry. Phase II: Stiffness decrease was followed with the plastic deformation of hole and composites initial damage occurred at the knee point where stiffness changed abruptly. In most samples, before stiffness and load recovery, evident load decline forming the first peak can be observed. Compared to the first phase, the curves ascend at a smaller slope accompanied with intermittent fluctuations indicating material damage occurring. It can be found that, with the increasing of W/D, E/D and D/t, the magnitude of the slope fluctuations augmented. This change can be mainly explained by that the single net tension, shearing out or cleavage failure mode show a stable load rising for type A, type D or type E, whereas bearing or multiple failure modes exhibit labile load variation for larger geometries. Phase III: The load gradually increased up to peak then suddenly drop, which reveals the joints lost the load carrying capability. It is can be seen respectively from the three groups of test results that the larger the geometry is, the larger ultimate load and longer the second phase can be obtained. For group 3, similar bearing failure modes and global shapes of the curves can be found, which reveals D/t has little effect on the failure mode. However, it is worth noting that, as the increase of D/t, the slope of curves in phase II and critical load rose obviously. This is mainly ascribed to the fact: the damaged material corresponding to the same degree of hole deformation increased. Furthermore, after the bearing initial failure, stiffness recovery observed is also related to the out-of-plane expansion of the damaged materials near the pin.

With the increase of D/t, more damaged materials quickly filled the gap between the composite plate and the fixture plates, which is known to lead to significant increase in bearing strength for laminates [21].

3.2 Damage mechanism

There are, in general, four basic joint failure patterns involving net-tension, shearing out, cleavage, and bearing referred to the composites in this research, although, sometimes combinations of these patterns occurred. The damage behavior in failure of pin-loaded satin woven C/C-SiC composites is complicated, particularly in the bearing failure including multiple damage mechanisms. Thus, further exploration of the occurrence and growth of the failure is obbligato to the damage tolerance evaluation of composite structures. To examine the accumulation and evolution of internal damage in detail during the experiments, microscopic images and AE signals including three features: amplitude, counting and energy of events were applied. The following discussion concentrates on the damage mechanism of representative failure modes in type A, C, D and E.

3.2.1 Net tension failure

Evolution of the amplitude, normalized cumulated counts and normalized cumulated energy of AE events for the type A together with the load-displacement curve and fractographic images were shown in Fig. 6 (a). In the beginning, besides noise seemed to be the influence of friction between the contact surfaces, AE signals are small, corresponding to an approximately linear elastic deformation with the stable mechanical performance of materials until the ultimate load. Accompanied by simple shapes of curves and small hole deformation, almost no damage near the hole and a flat and smooth hole edge can be observed for this type as shown in Fig. 6 (b). At the point of peak load, the energy and the counting increase dramatically, revealing serious damage including the most remarkable longitudinal fiber fracture with the amplitude close to 100dB, fiber/matrix interface debonding with the amplitude of 60-70dB, fiber pulling-out with the amplitude of 70-80dB and matrix cracking with the amplitude below 60dB, which resulting in the net tension failure.

3.2.2 Shearing out failure

As to type D, after the linear phase, the first sharp rising in the AE signal records at the knee point of the load-displacement curve reveals the distinct loss of stiffness and initial damage. Due to the small value of E/D, the stiffness transition is mainly attributed to the large number of matrix shearing cracking of 45-60 dB and weft yarn bending and debonding of 60-80 dB from hole edge to end surface along the shear-out planes, other than local bearing failure of hole edge. This can be also characterized the small hole deformation and relatively flat hole edge as shown in Fig. 7. Subsequently, the previously smooth load-displacement curve is replaced by an obvious but short fluctuation indicating more and more damage occurring, and the energy and event counting increase continuously but with the low amplitude. This is explained as: before the transverse fibers fracture, the main damage of this fluctuation phase is a large number fiber/matrix debonding and weft yarn bending with amplitude of below 80dB. When reaching the

ultimate load, drop of load is dominated by transverse fiber fracture with high amplitude beyond 80dB, accompanied by further interface debonding and fiber bending.

3.2.3 Cleavage failure

For type E, the flat and smooth hole edge can be found, which is similar to type D, but the sudden dramatic rising of AE signals corresponding to the initial damage reveals a gentle falling of stiffness. The subsequent fluctuation phase is longer than that of type D and the energy and event counting increase at a roughly uniform speed. This difference can be interpreted by the fact that, under the pressure of the pin, bending deformation occurred on the part of the composite plate from hole edge of to end face as shown in Fig. 8. According to the beam bending theory, the maximum tensile stress appeared at the center of the end face and the maximum compressive stress at the hole edge, leading to the weft yarn tension fracture and bulking to compression fracture. Additionally, the bending is featured by a progressive damage process along the center line of the plate with fiber fracture beyond 80dB and mass of matrix cracking below 60dB, corresponding to the gradual accumulation of the energy and event counting, until the cleavage failure is completed.

3.2.4 Full bearing failure

The net tension, shearing out and cleavage refer to situation wherein the load carrying capacity of the joints lost within a short time, while the bearing is widely deemed to be a desirable failure mode since the capacity to transfer load can be maintained longer. The progressive bearing failure can show a warning which significantly improves structure safety, and is recommended by designers. Compared with net tension, shearing out and cleavage, bearing behavior is relatively complicated and characterized by multiple failure mechanisms. For bearing failure, as shown in Fig. 9, low AE data values have been recorded in early phase during the experiment. Subsequently, the significant rising in AE signal records reveals the first loss of linearity and the energy and event counting increase with undulation but at a relatively stable rate, indicating multiple progressive damage occurring. For examining the features of bearing damage better, micrograph images were taken in corresponding failure morphology of different views including hole edge, pin contact surface and middle cut plane as shown in Fig. 10 – Fig. 12 (the white dotted line is the center line of the bolt in Fig. 10 and the green represents the pin in Fig. 12 during the experiments), and the load levels of type C were divided into about 75%, 85% and 100% of the maximum load. Bearing damage initiatively occurred at the hole edge and then propagated unstably in the plate. Due to the brittleness matrix of C/C-SiC composites, partial damaged material was crushed to fragments and fell off. In Fig. 10 (a), The first observation obtained is very localized damage at the contact surface in front of the loaded hole boundary resulting from micro-damage mainly including warp and weft yarns micro-buckling and splitting, matrix crushed and slight fiber/matrix interface debonding at the level of 75%. Thus, high-amplitude AE signals about 80 dB corresponding to the yarns splitting are mixed with middle-amplitude ones of 60-80 dB representing the yarns buckling and interface damage and low-amplitude ones of 45-60 dB showing the matrix damage. Thereinto the fiber bundles buckling and splitting close to the hole primarily accounted for the initial damage at the knee point of load–

displacement curve. It is can be also noticed that partial damaged materials near the hole edge were pushed outwards to form bulge as illustrated in Fig. 11 (a). When the load increased to 85% of the maximum load, the damage region developed more extensively in front of the hole boundary and hole deformation augmented, but still extended over a limited area in front of the hole edge, which is visibly found from the middle cut plane view in Fig. 12 (b). Except for the further weft yarns bending to fracture and warp yarns crushed breakage, the fiber/matrix interface debonding became serious, propagating transversely and longitudinally and leading to delamination on the layers outside. Therefore, the counts of middle-amplitude signals of 60-80 dB indicating fiber/matrix and delamination increased. At the level of the maximum load, yarns failure and delamination aggravated and damaged yarns arrangement became disorganized. Particularly, the delamination occurred inside of the plate as shown in Fig. 12 (c). In research [11] on bearing failure of laminate, the aggravation of fiber buckling and through-thickness shearing action generated angular shear cracks and large-scale delamination through the thickness of the specimen at this level. However, for the composites in this research, fiber damage was more local and the delamination occurred gradually from outside to inside along the thickness of the plate. Actually, weft yarns and warp yarns were forced to break by a combination of compressive and out-of-plane action, so that for satin woven composites with original fiber bundles bending, yarns crushed buckling and debonding tended to appear near the pin compared with the laminate. While due to a long hole deformation, E/D was small enough to meet the secondary cleavage failure mode. Thus, subsequent fiber and matrix fracture under tension and compression, accompanied by a sudden increase in number of high-amplitude signals beyond 80 dB and a load drop, was found to begin at the center of the hole edge and run directly through the end surface, which was similar to the damage mechanisms of type E mentioned above.

The AE amplitude ranges for the matrix cracking, interface debonding fiber pulling-out and fiber fracture are respectively about 45–60 dB, 60-70 dB, 70–80 dB, and 80–100 dB, which are basically consistent with those of the carbon fiber/epoxy composite laminates by Liu et al. [22] and the self-reinforced polyethylene composites by Zhuang et al. [23] as shown in Fig. 13. The main difference may lie in fibrous preform woven form. In addition, Bohse [24] used release rate of AE events energy and Groot et al. [25] used AE peak frequency to monitor damage mechanisms. Although AE parameters selected to apply in the investigation are different, the relative signals ranges corresponding to the damage mechanisms are generally consistent. However, comprehensive understanding of the damage mechanisms may require further in-depth insight.

4. Conclusions

This research focuses on the experiment details of failure behavior for 5HS woven C/C-SiC composites under pin-loading. The effects of geometries on the mechanical response and failure modes were obtained. Combining AE testing, the evaluation of damage mechanism for four basic failure modes was discussed. Some conclusions and observations derived from the investigation are summarized as follows:

1. Except for type A showing a linear elastic and brittle fracture shape, the load–displacement curve for each type can be divided into three phases, which represent linear elasticity, damage onset and growth and final structural failure. In each group, the ultimate load and fluctuation of the second phase increased with the geometry increase. The failure mode was respectively found as net tension, combination of net tension and slight bearing, and full bearing when W/D was equal to 2, 3.5 and 5. The failure mode was shearing out, cleavage, and full bearing when W/D was equal to 1.5, 2.5 and 3.5. Full bearing failure modes occurred alike when D/t was equal to 1.2, 1.6 and 2.
2. The net tension failure for type A was caused by initial slight bearing damage including yarn bending and breakage, matrix crushed and final tensile damage including yarn and matrix fracture. The shearing out failure for type D was mainly attributed to abundant matrix cracks and weft yarn debonding and breakage in a short time. The cleavage failure for type E was resulted from bending damage including the weft yarn tension fracture and bulking to compression fracture. The full bearing failure for type C was due to more complex but local damage including matrix crushed, yarns debonding and fracture fiber/matrix interface debonding gradually resulting in delamination. Correlations between the damage mechanisms and the acoustic emission amplitude ranges were partially described as that the matrix cracking, interface debonding, fiber pulling-out and fiber breakage matched respectively about 45–60 dB, 60-70 dB, 70–80 dB, and 80–100 dB.

Declarations

Declaration of Conflicting Interests

The author(s) declared no potential conflicts of interest with respect to the research, authorship, and/or publication of this article.

Acknowledgments

This work was supported by the National Natural Science Foundation of China under Grant No. 11572101.

References

[1] Swolfs Y, Verpoest I, Gorbatikh L. A review of input data and modelling assumptions in longitudinal strength models for unidirectional fibre-reinforced composites. Compos Struct 2016, 150: 153–172.

[2] Maples HA, Wakefield S, Robinson P, Bismarck A. High performance carbon fibre reinforced epoxy composites with controllable stiffness. Compos Sci Technol 2014, 105: 134–143.

[3] Zhao L, Xin A, Liu F, Zhang J, Hu N. Secondary bending effects in progressively damaged single-lap, single-bolt composite joints. Results Phys 2016, 6: 704-711.

[4] Asi O. An experimental study on the bearing strength behavior of Al2O3 particle filled glass fiber reinforced epoxy composites pinned joints. Compos Struct 2010, 92: 354–363.

[5] Olmedo A, Santiuste C. On the prediction of bolted single-lap composite joints. Compos Struct 2012, 94: 2110–2117.

[6] Collings TA. The strength of bolted joints in multi-directional CFRP laminates. Composites 1977, 8: 43–55.

[7] Chang FK, Scott RA, Springer GS. Strength of mechanically fastened composite joints. J Compos Mater 1982, 16: 470-494.

[8] Aktas A, Karakuzu R. Failure Analysis of two-dimensional carbon-epoxy composite plate pinned joint. Mech Compos Mater Struct 1999, 6: 347–361.

[9] Okutan B. The effects of geometric parameters on the failure strength for pin-loaded multi-directional fiber-glass reinforced epoxy laminate. Composites Part B 2002, 33: 567–578.

[10] Camanho PP, Bowron S, Matthews FL. Failure mechanisms in bolted CFRP. J Reinf Plast Compos 1998, 17: 205-233.

[11] Xiao Y, Ishikawa T. Bearing strength and failure behavior of bolted composite joints (part I: Experimental investigation). Compos Sci Technol 2005, 65: 1022–1031.

[12] Eriksson I. On the bearing strength of bolted graphite/epoxy laminates. J Compos Mater 24 1990, 24: 1264–1269.

[13] Okutan B, Aslan Z, Karakuzu R. A study of the effects of various geometric parameters on the failure strength of pin-loaded woven-glass-fiber reinforced epoxy laminate. Compos Sci Technol 2001, 61: 1491–1497.

[14] Karakuzu R, Gulem T, Icten BM. Failure analysis of woven laminated glass–vinylester composites with pin-loaded hole. Compos Struct 2006, 72: 27–32.

[15] Buckley JD, Edie DD. Carbon-carbon materials and composites. Noyes Publications: New Jersey, NJ, USA, 1993.

[16] Khan Z, Alsulaiman FS, Farooqi JK. Fatigue damage characterization in plain-weave carbon-carbon fabric reinforced plastic composites. J Reinf Plast Compos 1998, 17: 1320-1337.

[17] Sharma R, Mahajan P, Mittal RK. Elastic modulus of 3D carbon/carbon composite using image-based finite element simulations and experiments. Compos Struct 2013, 98: 69–78.

[18] Kogo Y, Kikkawa A, Saito W, Hatta H. Comparative study on tensile fracture behavior of monofilament and bundle C/C composites. Composites Part A 2006, 37: 2241-2247.

[19] Cheng J, Li H, Zhang S, Xue L, Luo W, Li W. Failure behavior investigation of a unidirectional carbon–carbon composite. Mater Des 2014, 55: 846–850.

[20] ASTM Standard D5961, Standard test method for bearing response of polymer

matrix composite laminates. ASTM International, West Conshohocken, PA, 2010.

[21] Mounien R, Fagiano C, Paulmier P, Tranquar Bt, Irisarri F-X. Experimental characterization of the bearing behavior of 3D woven composites. Composites Part B 2017, 116: 369-376.

[22] Liu PF, Chu JK, Liu YL, Zheng JY. A study on the failure mechanisms of carbon fiber/epoxy composite laminates using acoustic emission. Mater Des 2012, 37: 228–235.

[23] Zhuang X, Yan X. Investigation of damage mechanisms in self-reinforced polyethylene composites by acoustic emission. Compos Sci Technol 2006, 66: 444-449.

[24] Bohse J. Acoustic emission characteristics of micro-failure processes in polymer blends and composites. Compos Sci Technol 2000, 60: 1213-1226.

[25] Groot PJ, Wijnen PAM, Janssen RBF. Real-time frequency determination of acoustic emission for different fracture mechanisms in carbon/epoxy composites. Compos Sci Technol 1995, 55: 405-412.

Figures

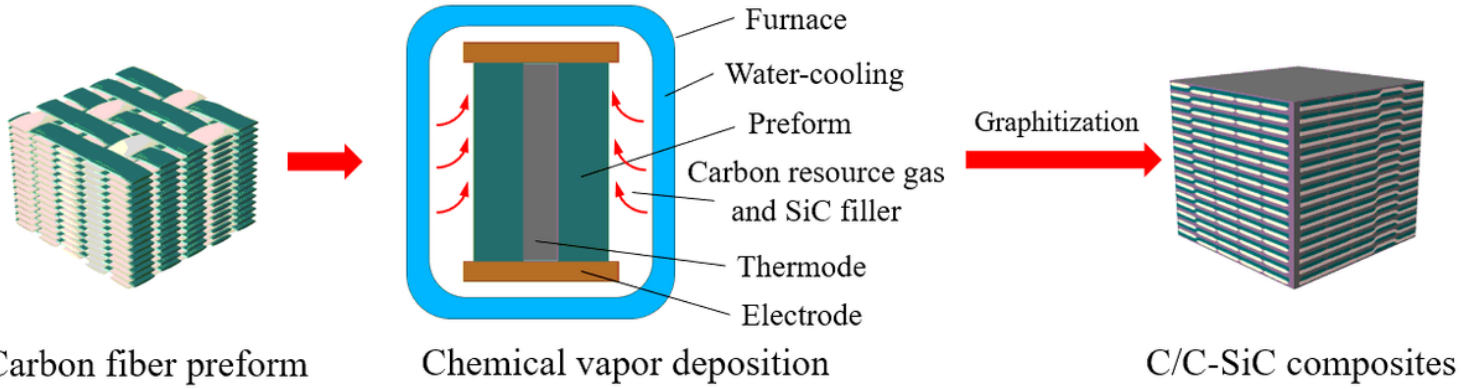

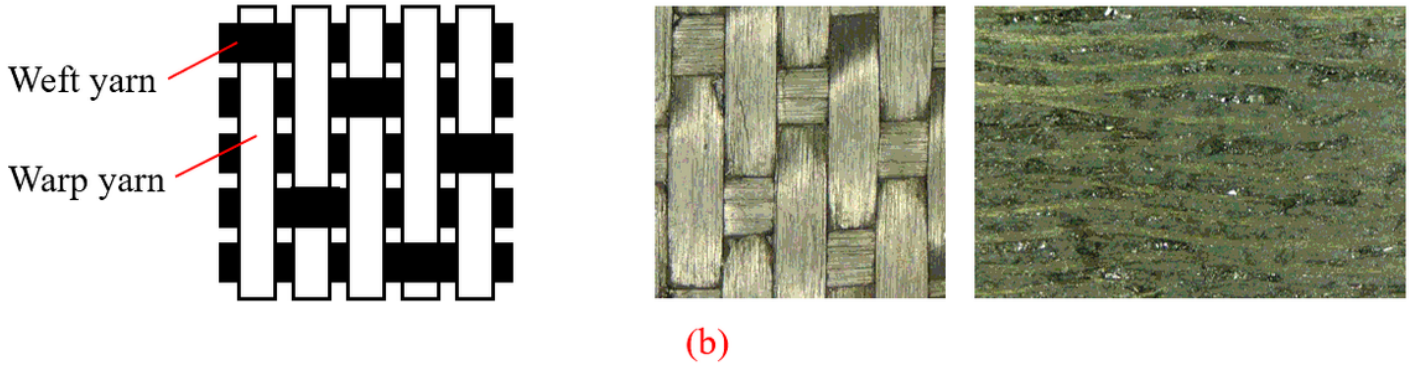

Figure 1

(a) Preparation process of C/C- SiC composites. (b) Fabric texture of the preform.

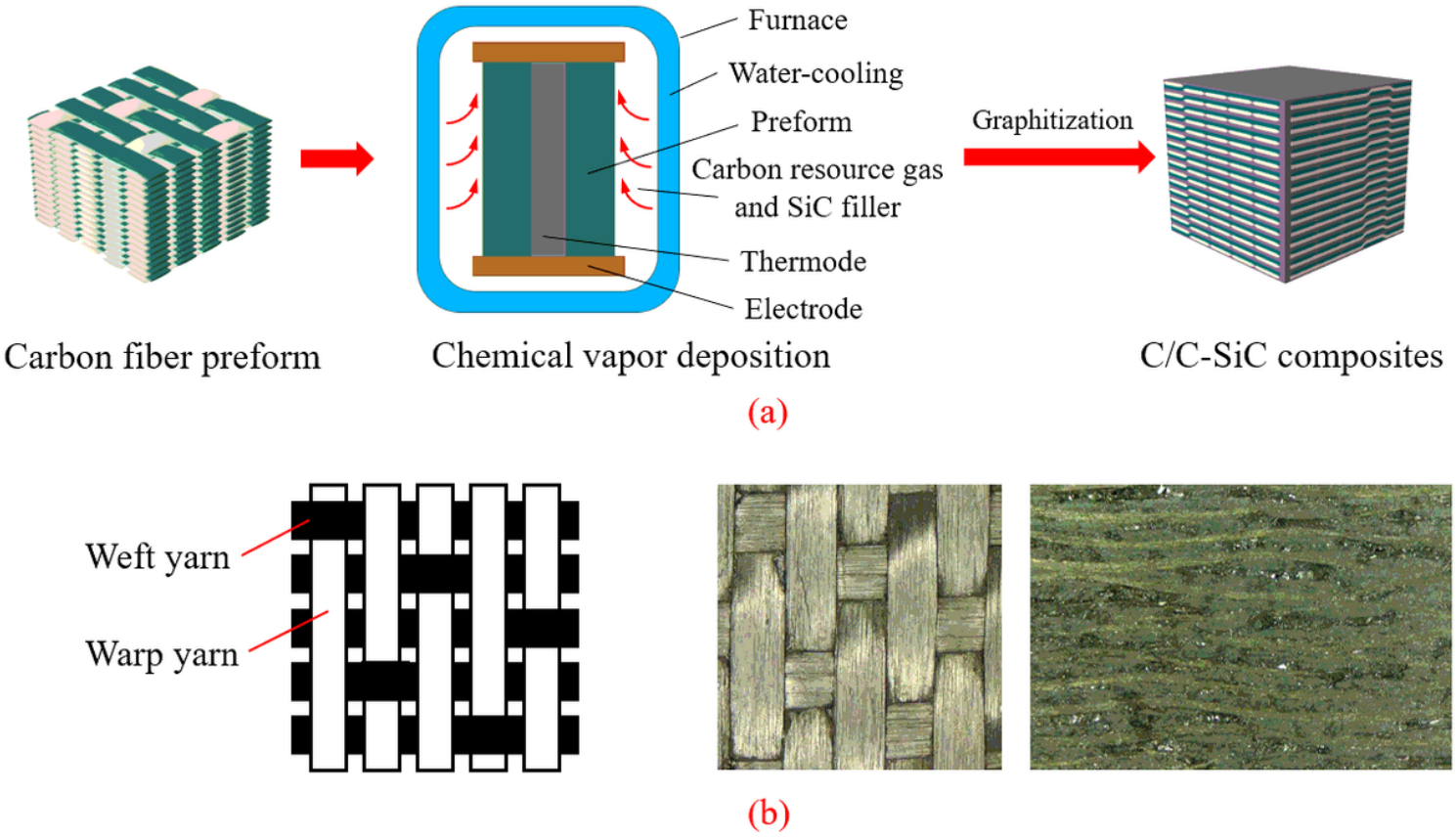

Figure 1

(a) Preparation process of C/C- SiC composites. (b) Fabric texture of the preform.

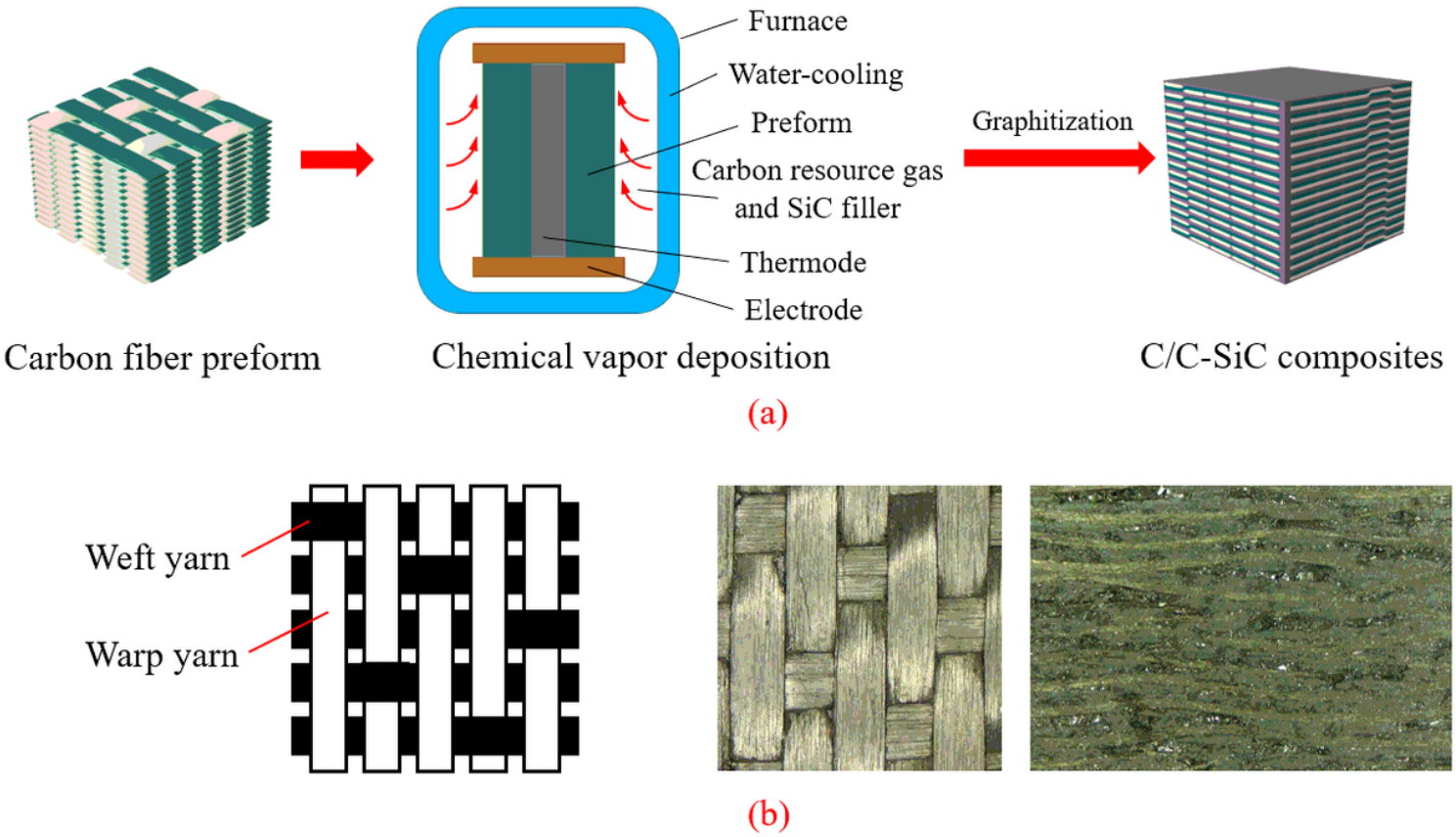

Figure 1

(a) Preparation process of C/C- SiC composites. (b) Fabric texture of the preform.

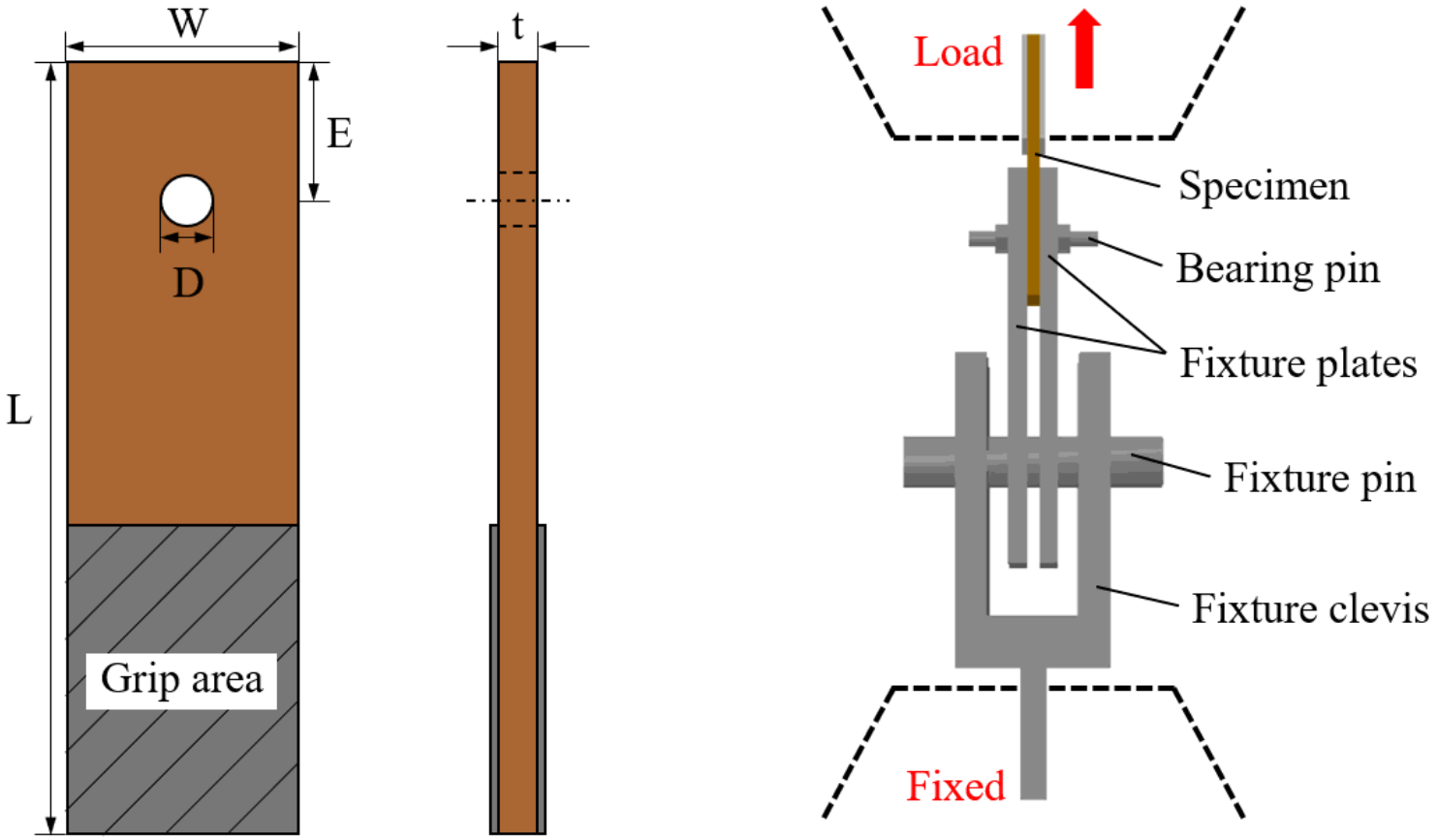

Figure 2

Geometrical configuration and testing setup of the pin-loaded specimen.

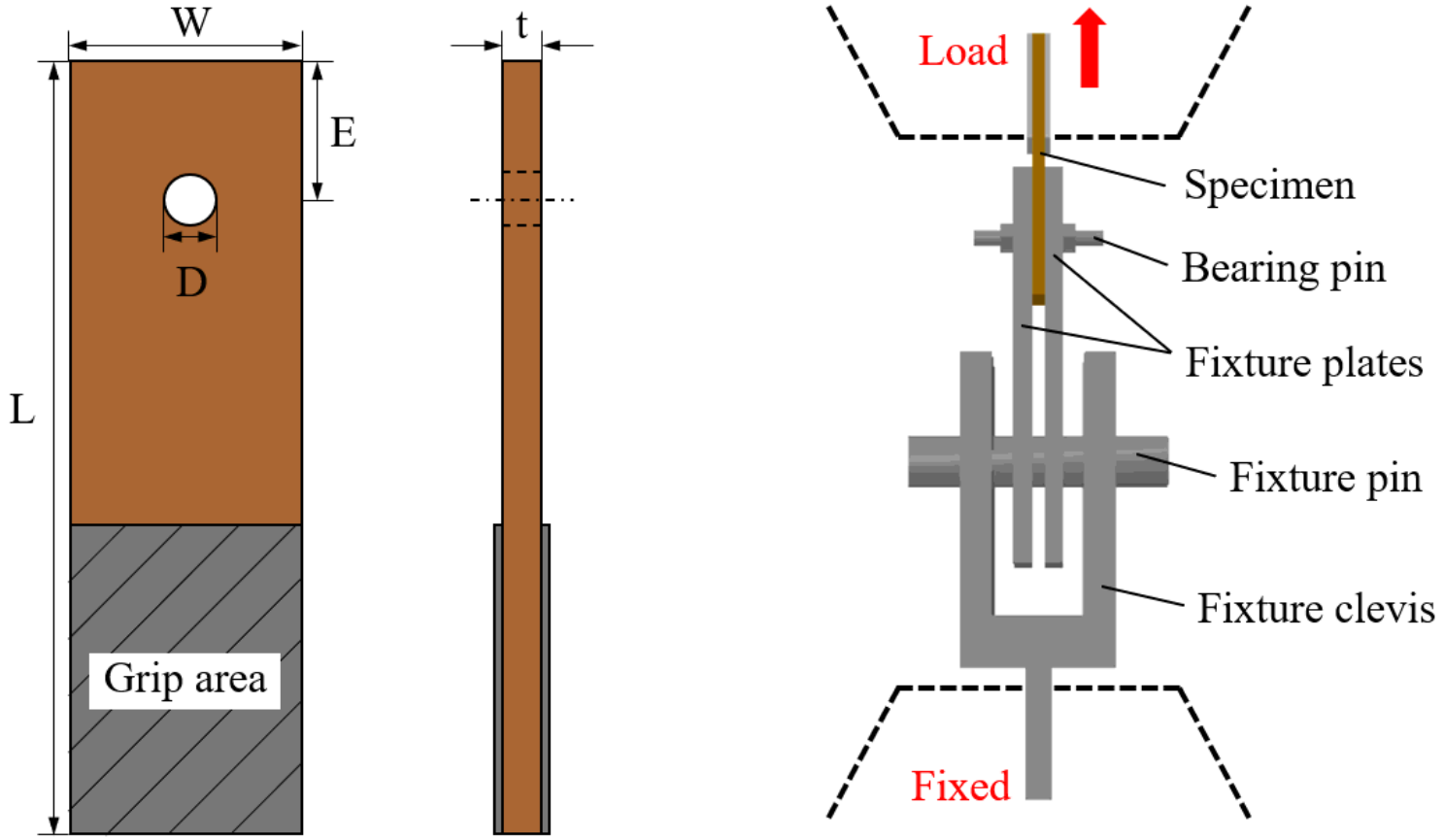

Figure 2

Geometrical configuration and testing setup of the pin-loaded specimen.

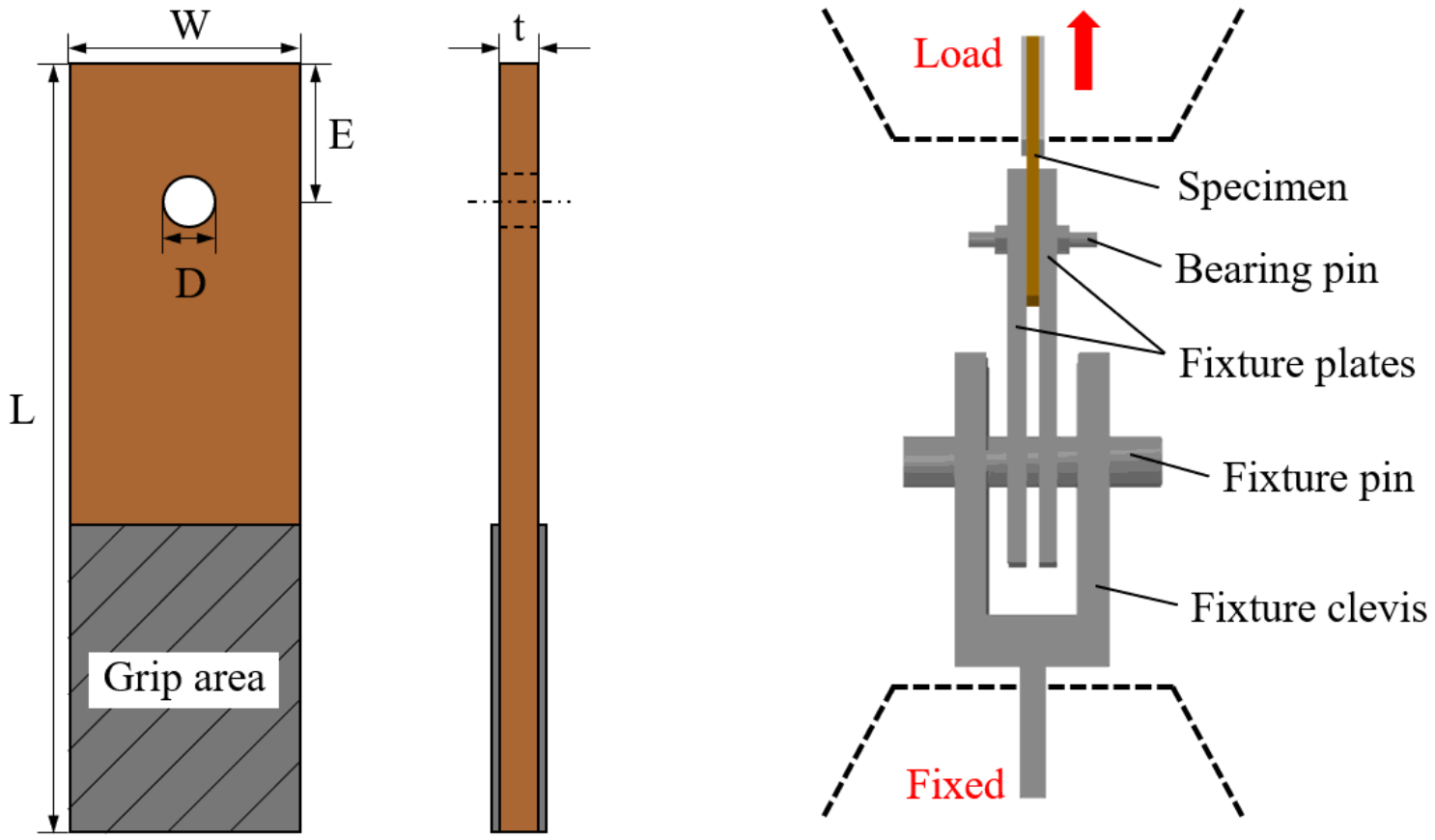

Figure 2

Geometrical configuration and testing setup of the pin-loaded specimen.

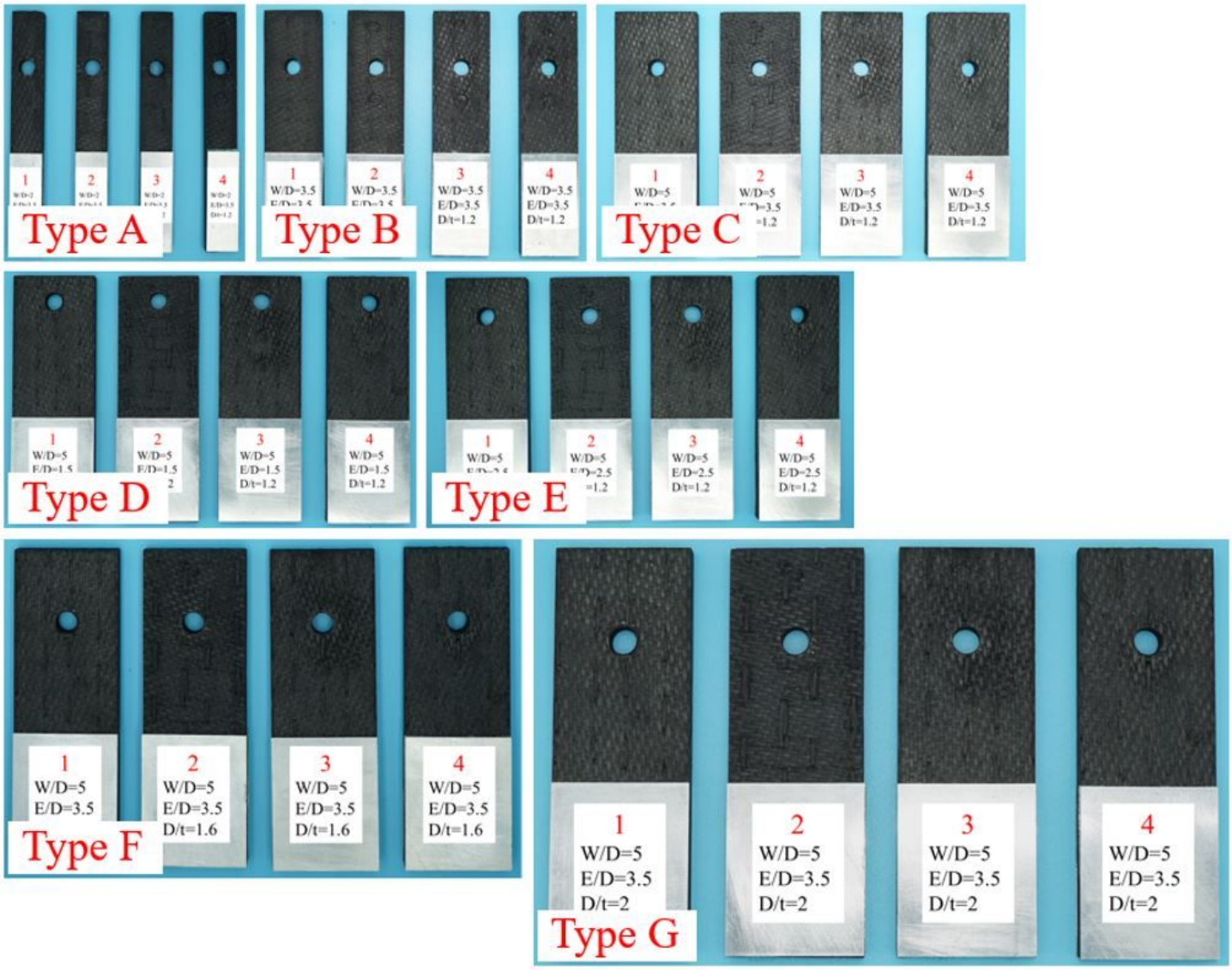

Figure 3

Seven types of the test pieces.

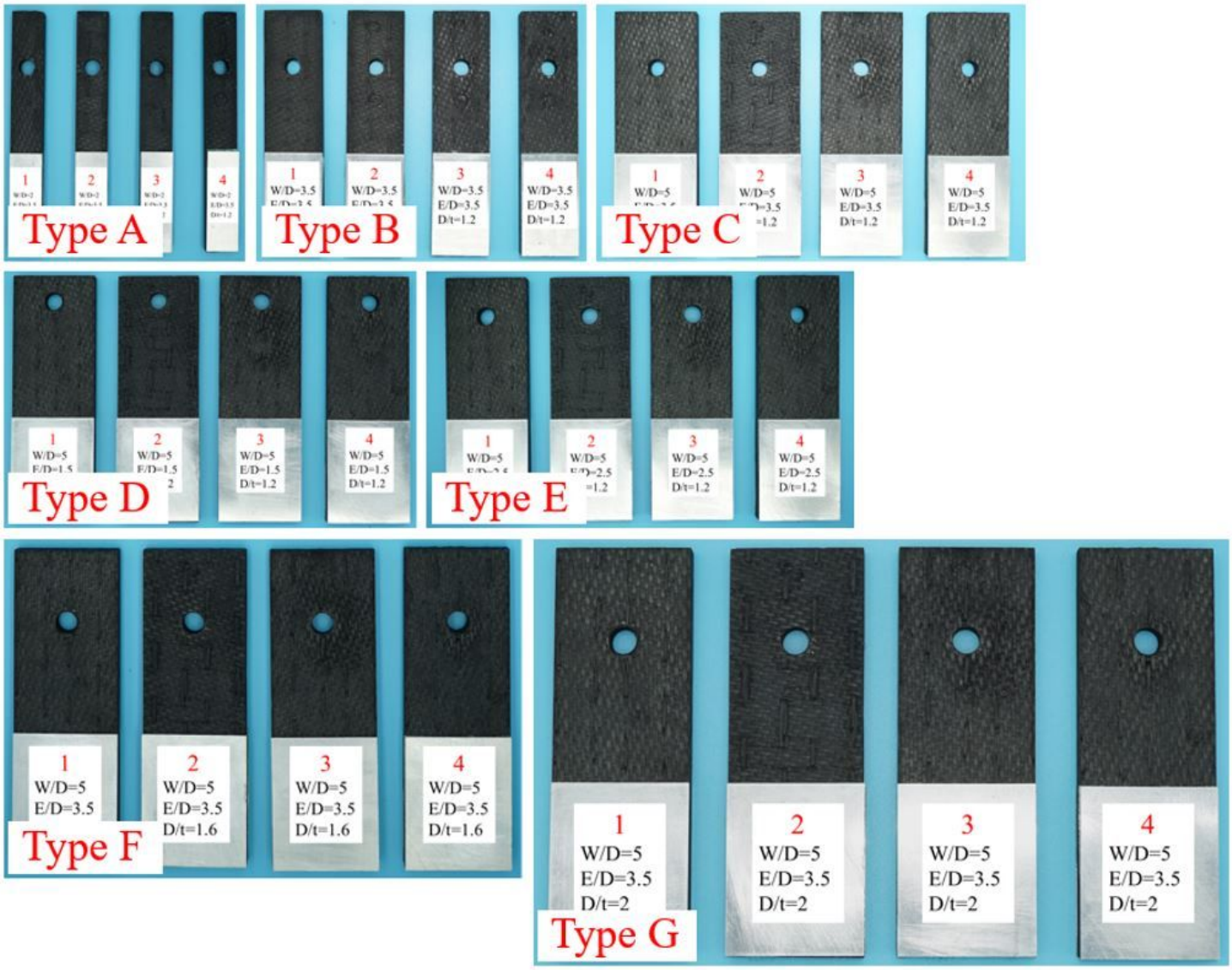

Figure 3

Seven types of the test pieces.

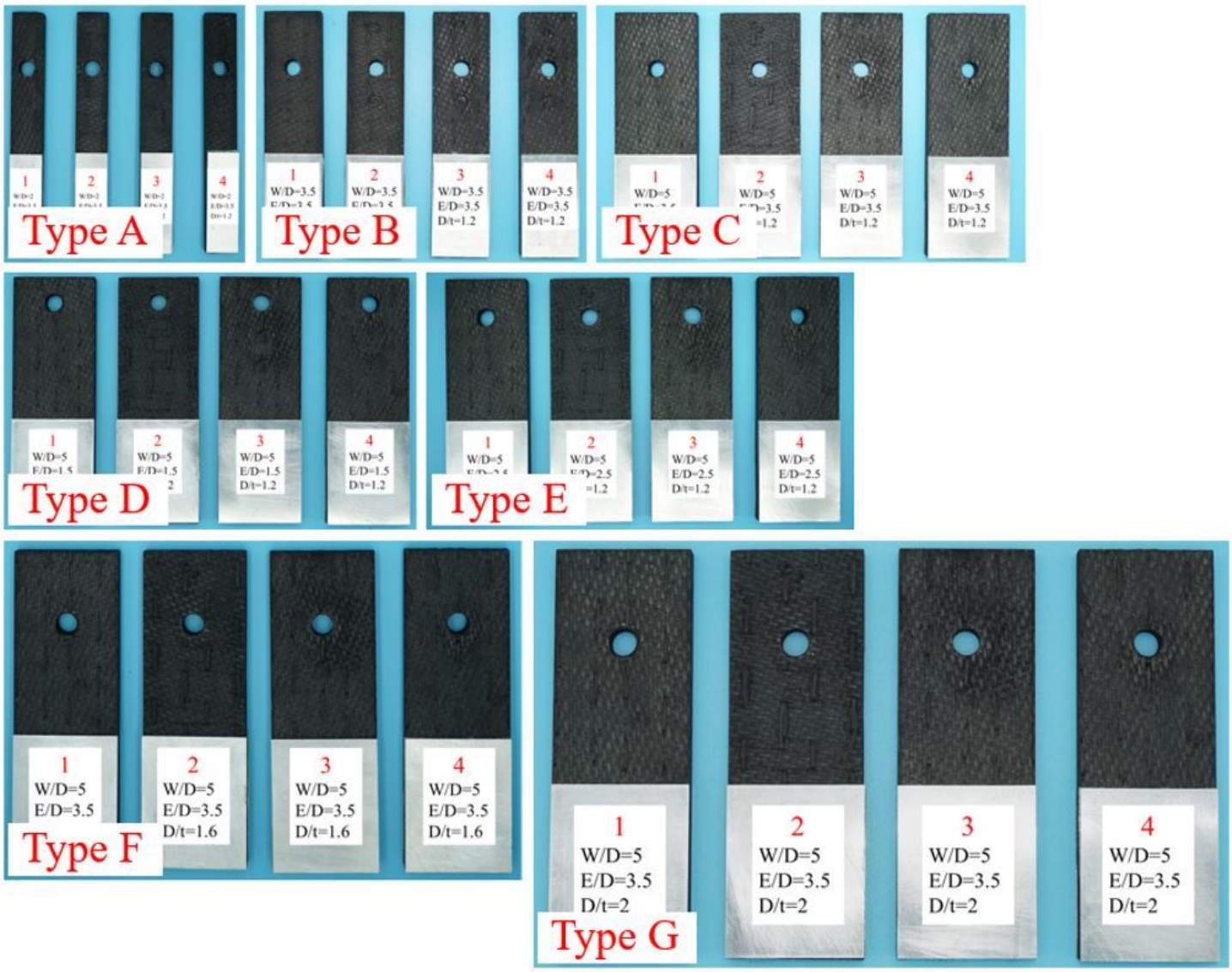

Figure 3

Seven types of the test pieces.

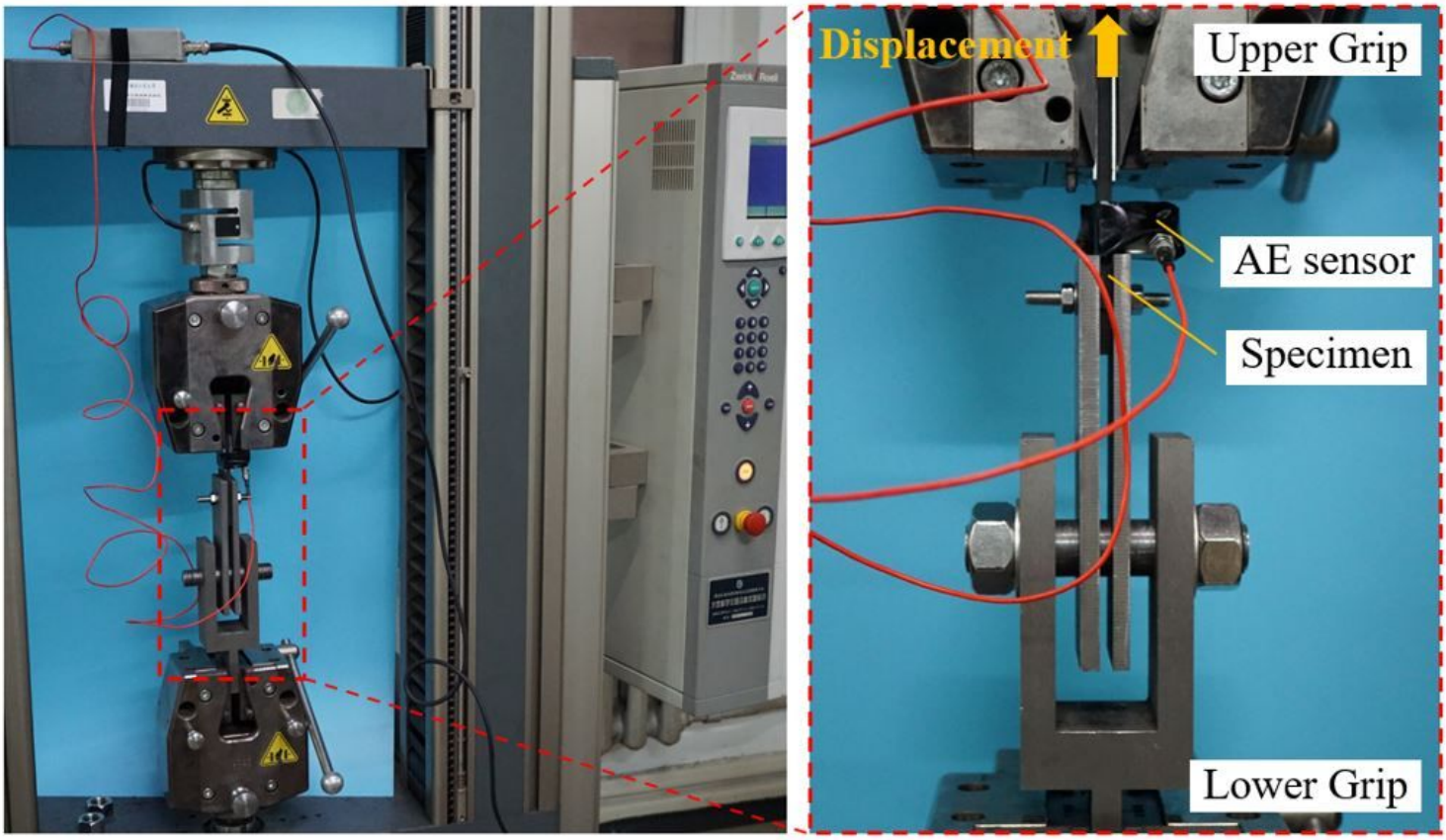

Figure 4

Measurement system of the single-bolt double-lap.

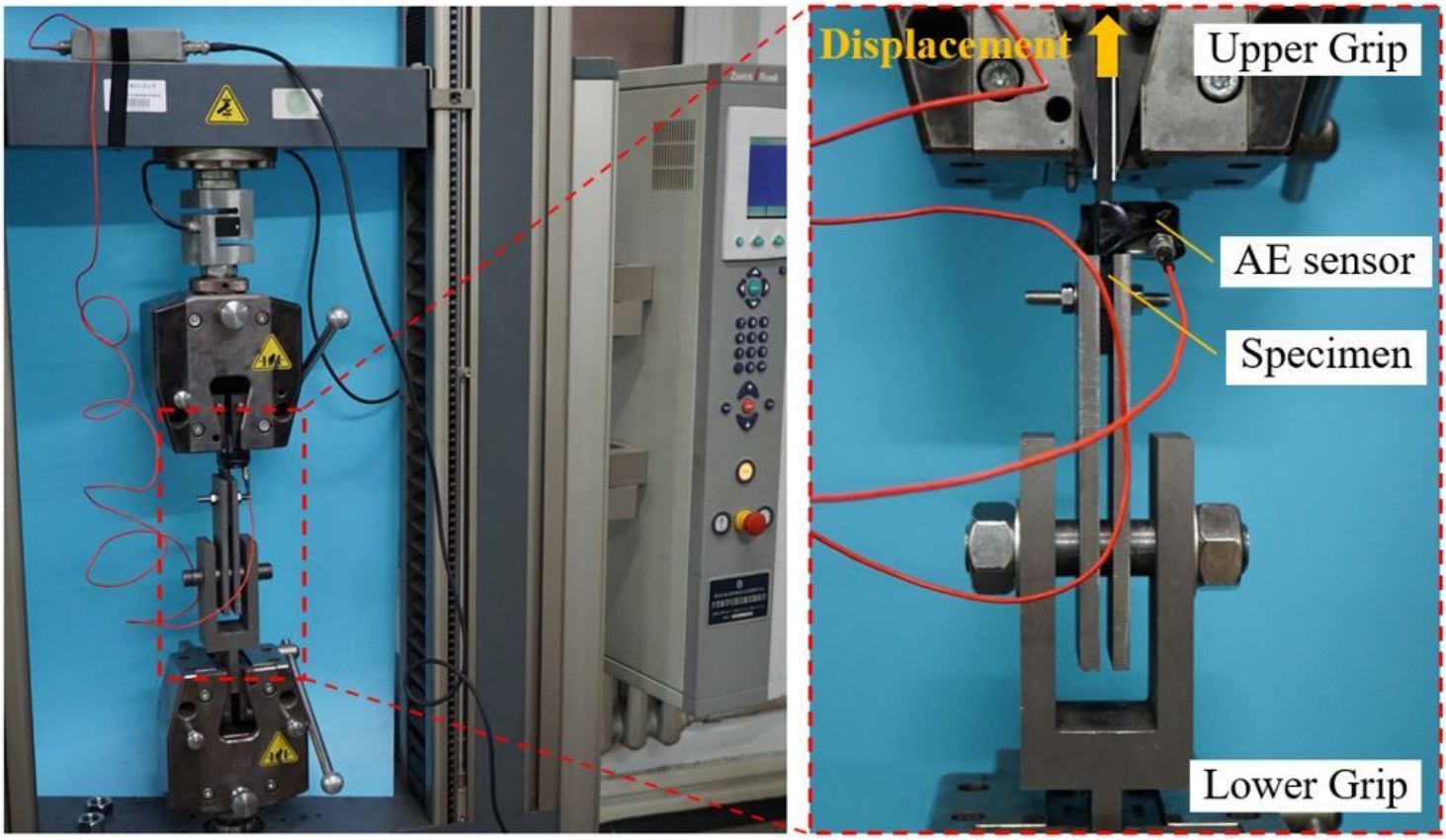

Figure 4

Measurement system of the single-bolt double-lap.

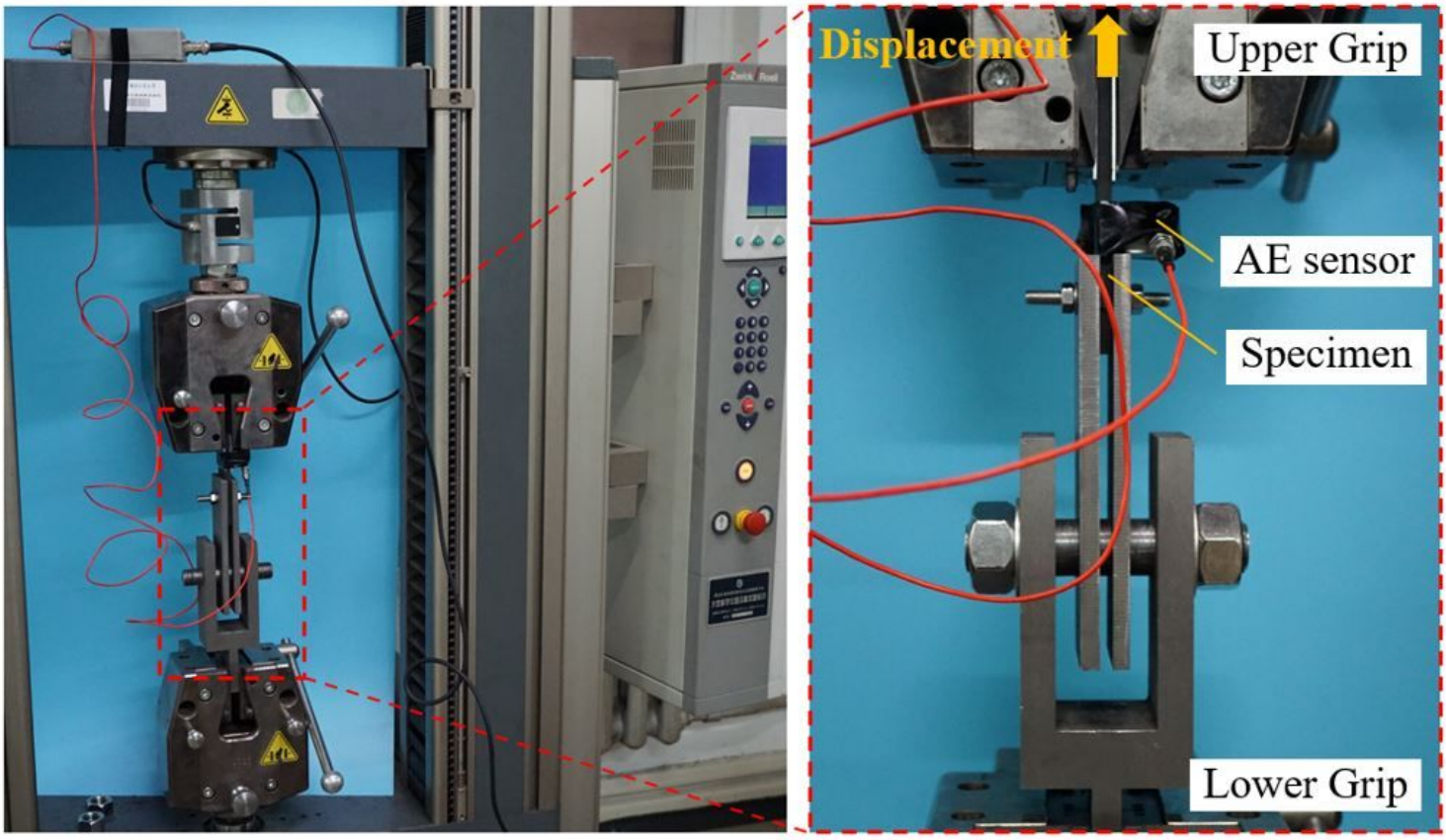

Figure 4

Measurement system of the single-bolt double-lap.

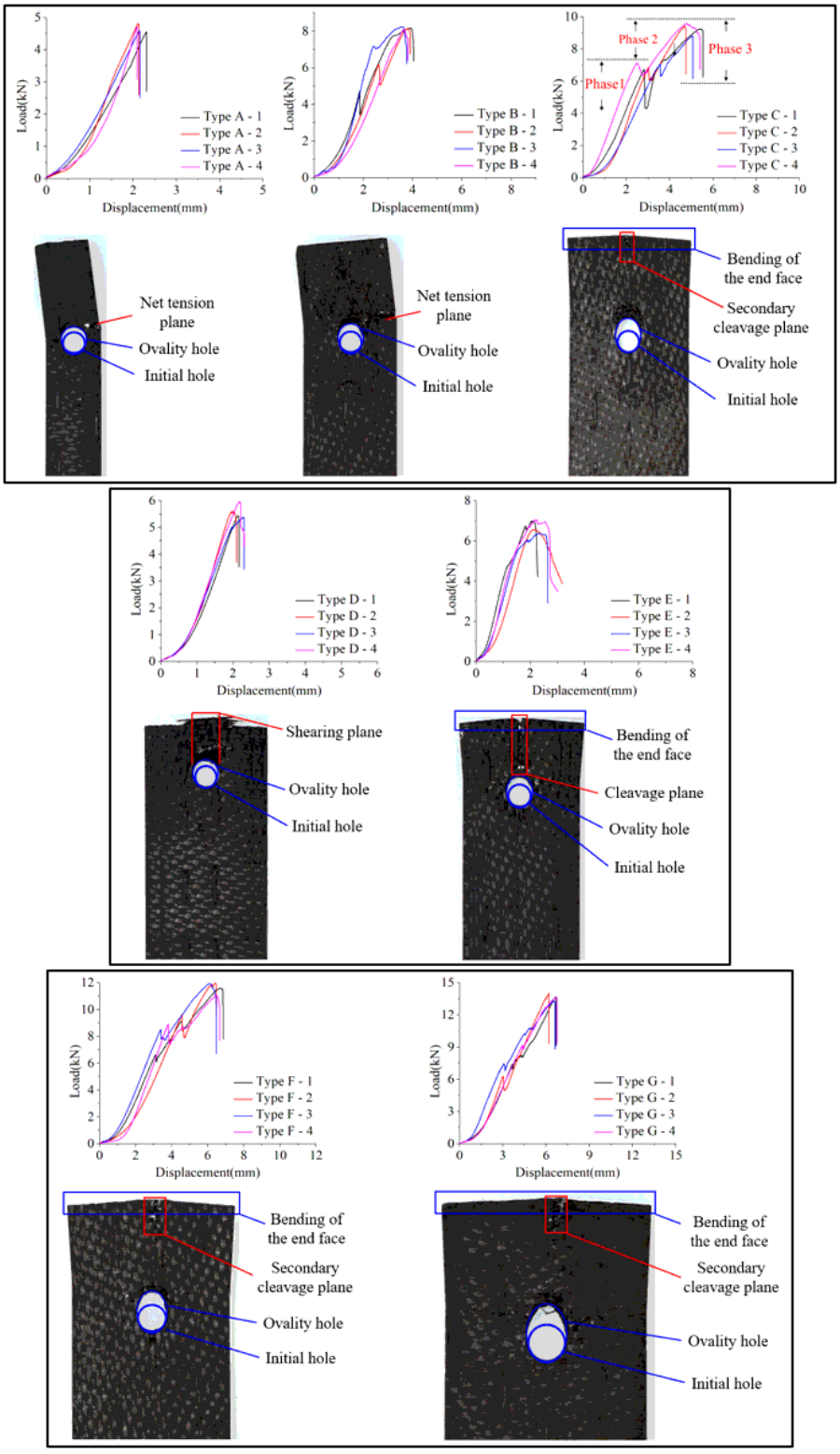

Figure 5

Failure modes and load–displacement curves.

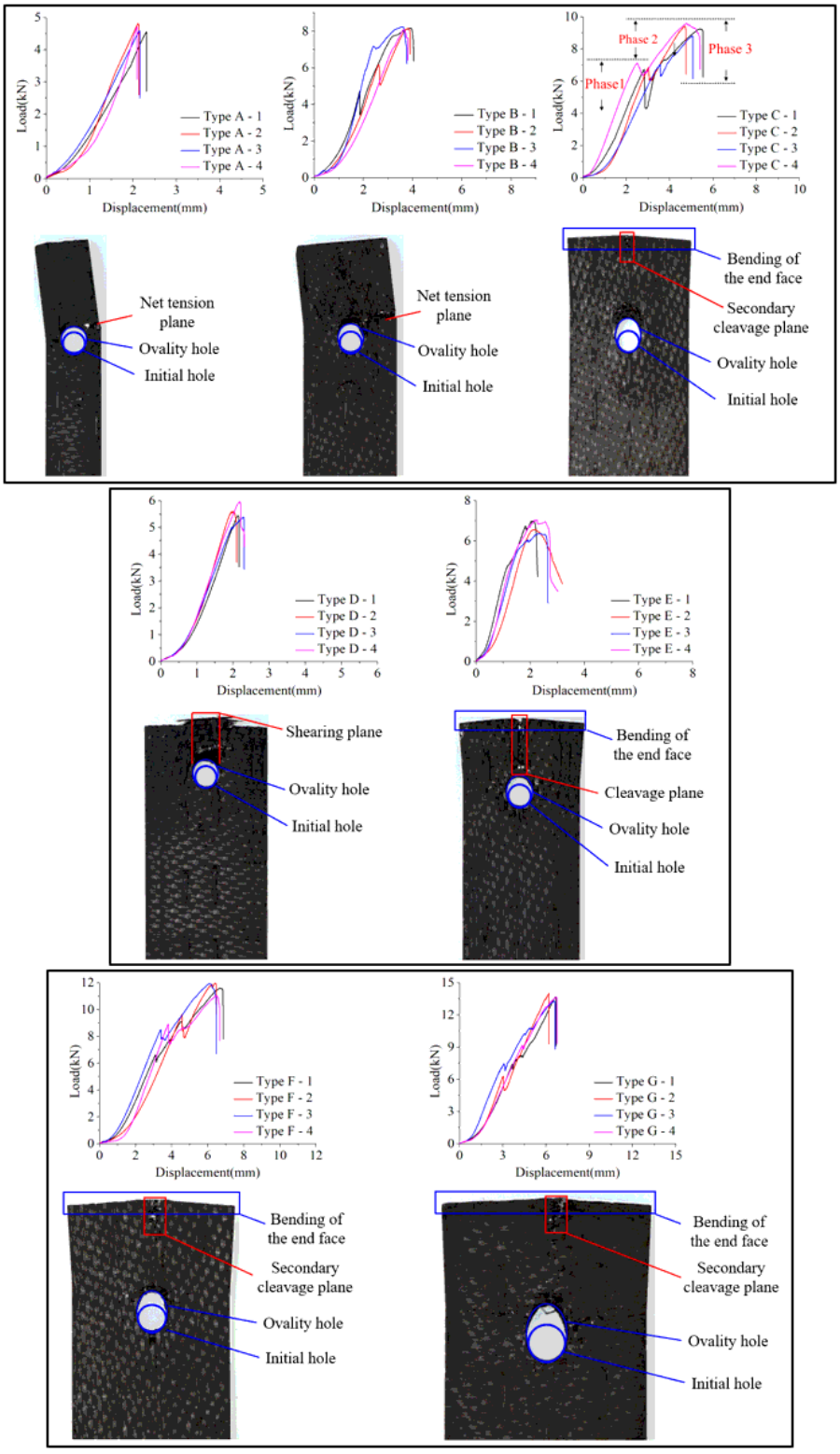

Figure 5

Failure modes and load–displacement curves.

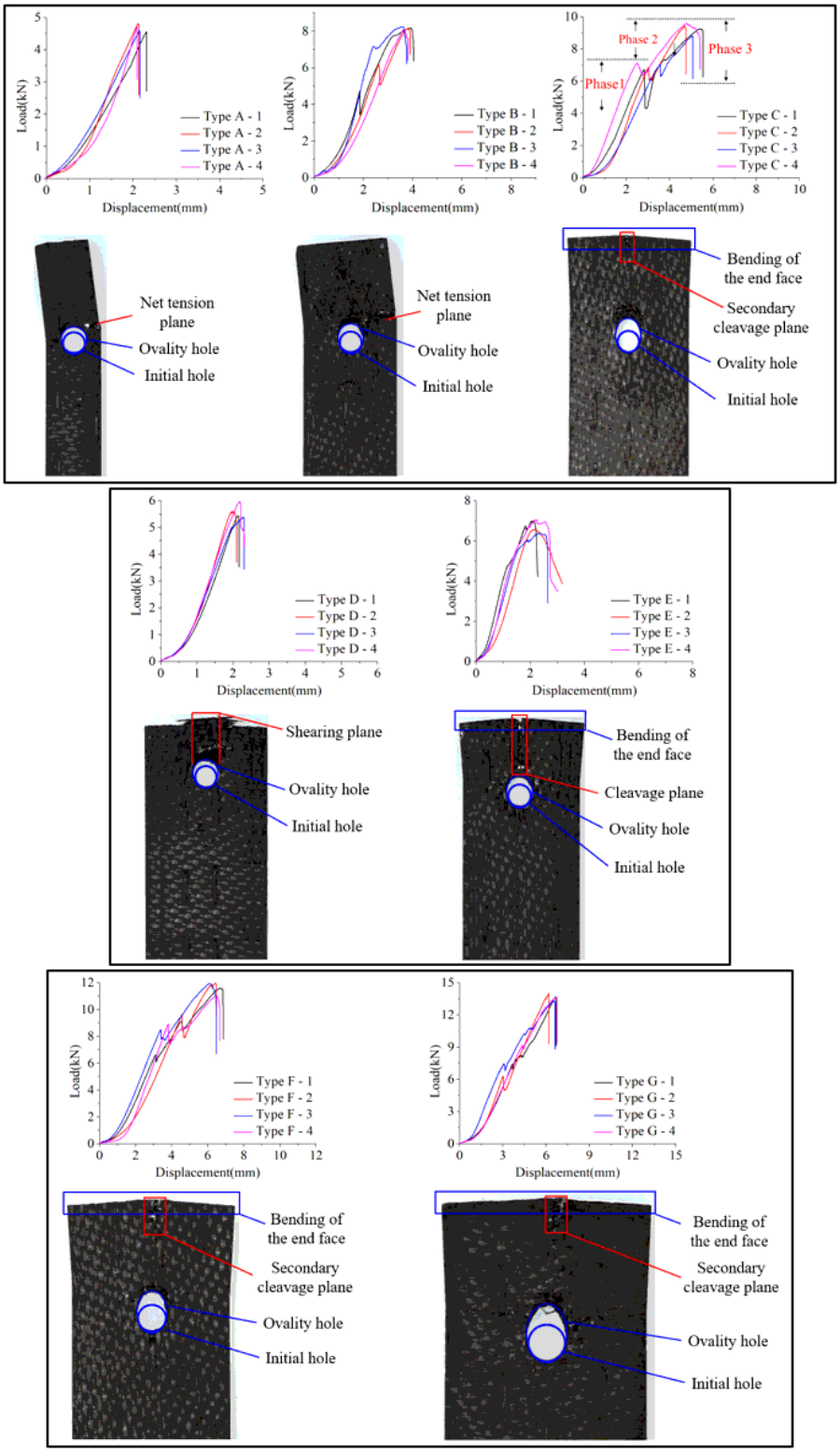

Figure 5

Failure modes and load–displacement curves.

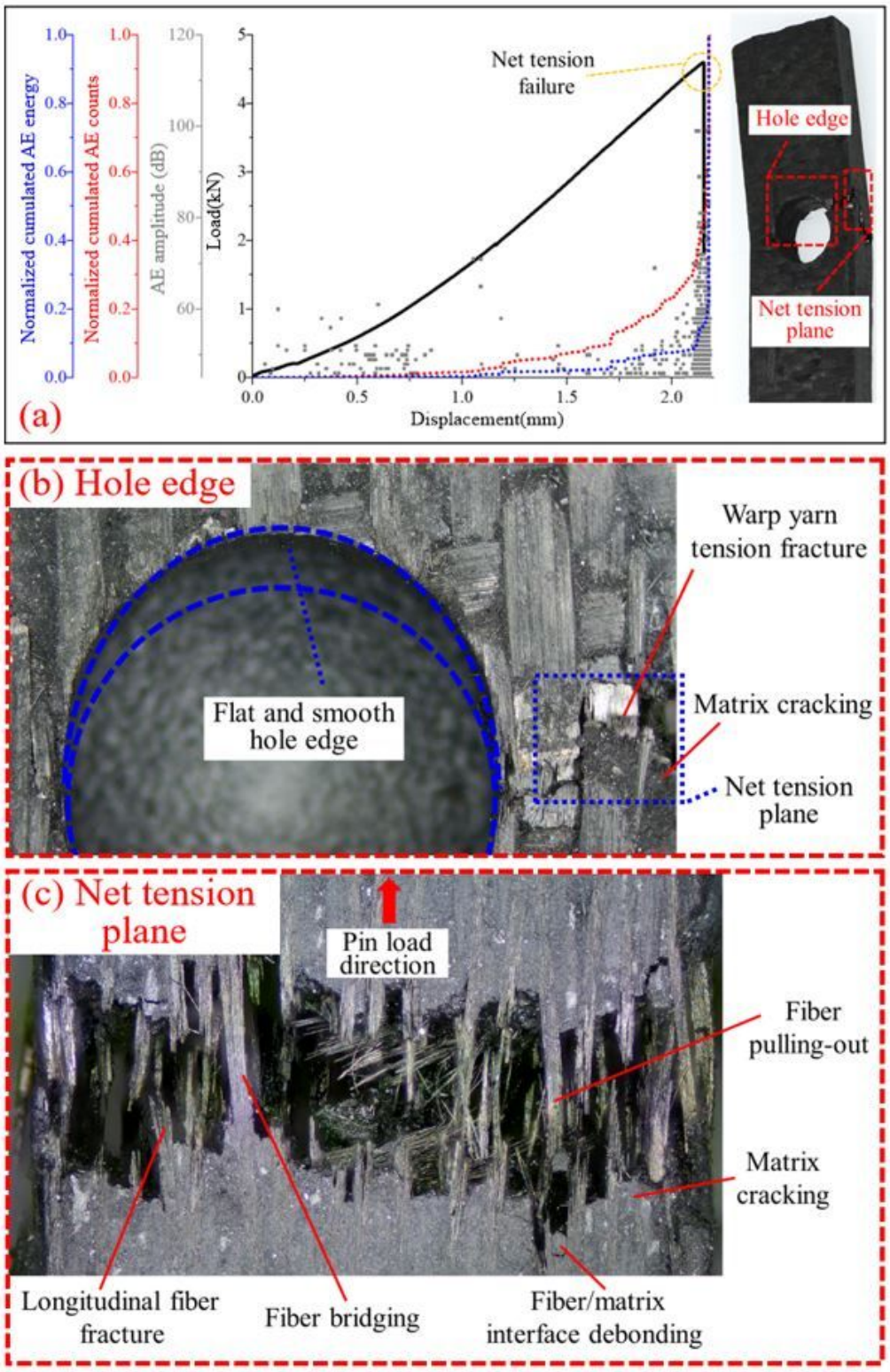

Figure 6

(a) Load and AE events vs. displacement curves and (b) morphology of the hole edge and (c) net tension plane for type A.

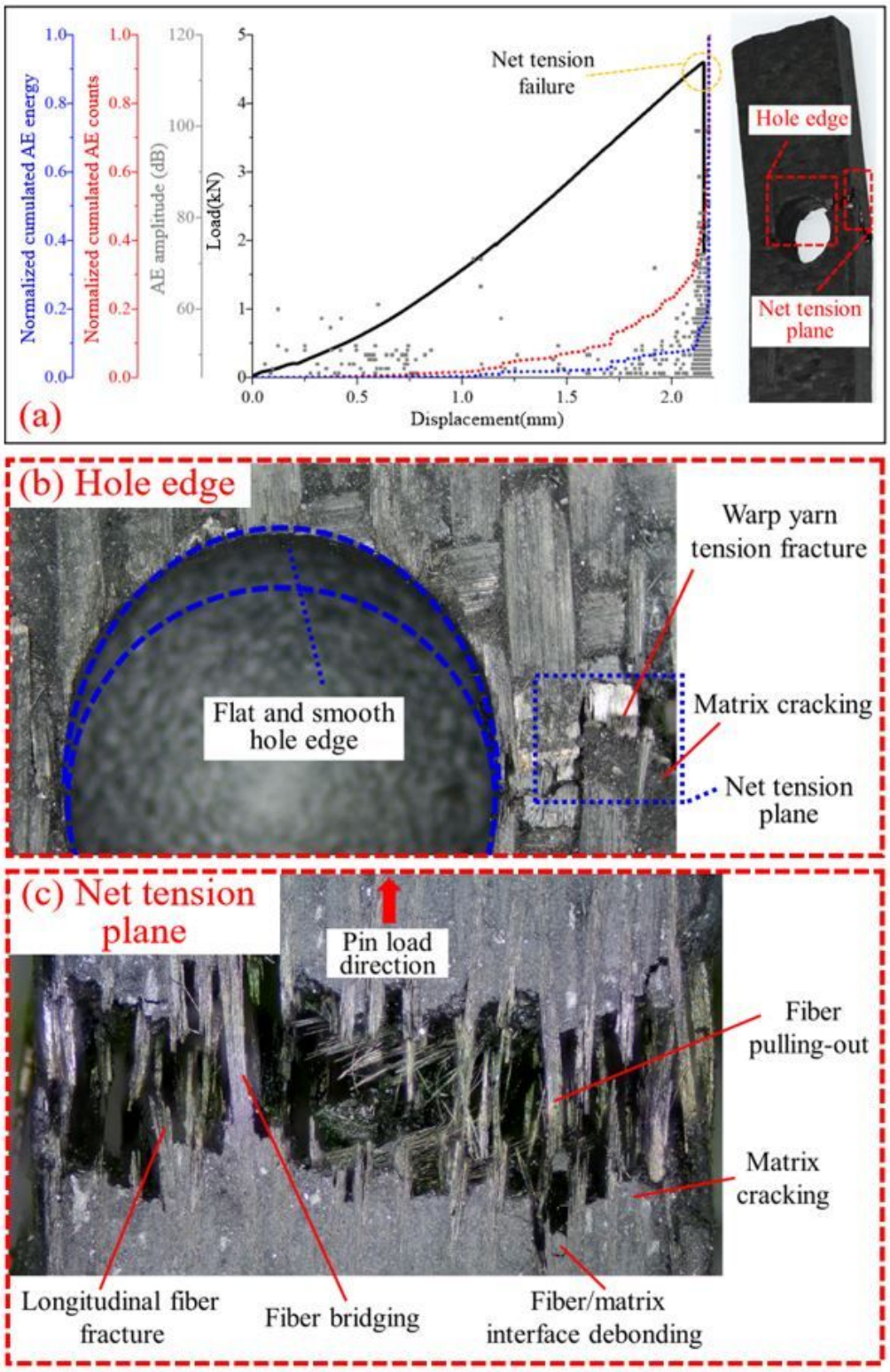

Figure 6

(a) Load and AE events vs. displacement curves and (b) morphology of the hole edge and (c) net tension plane for type A.

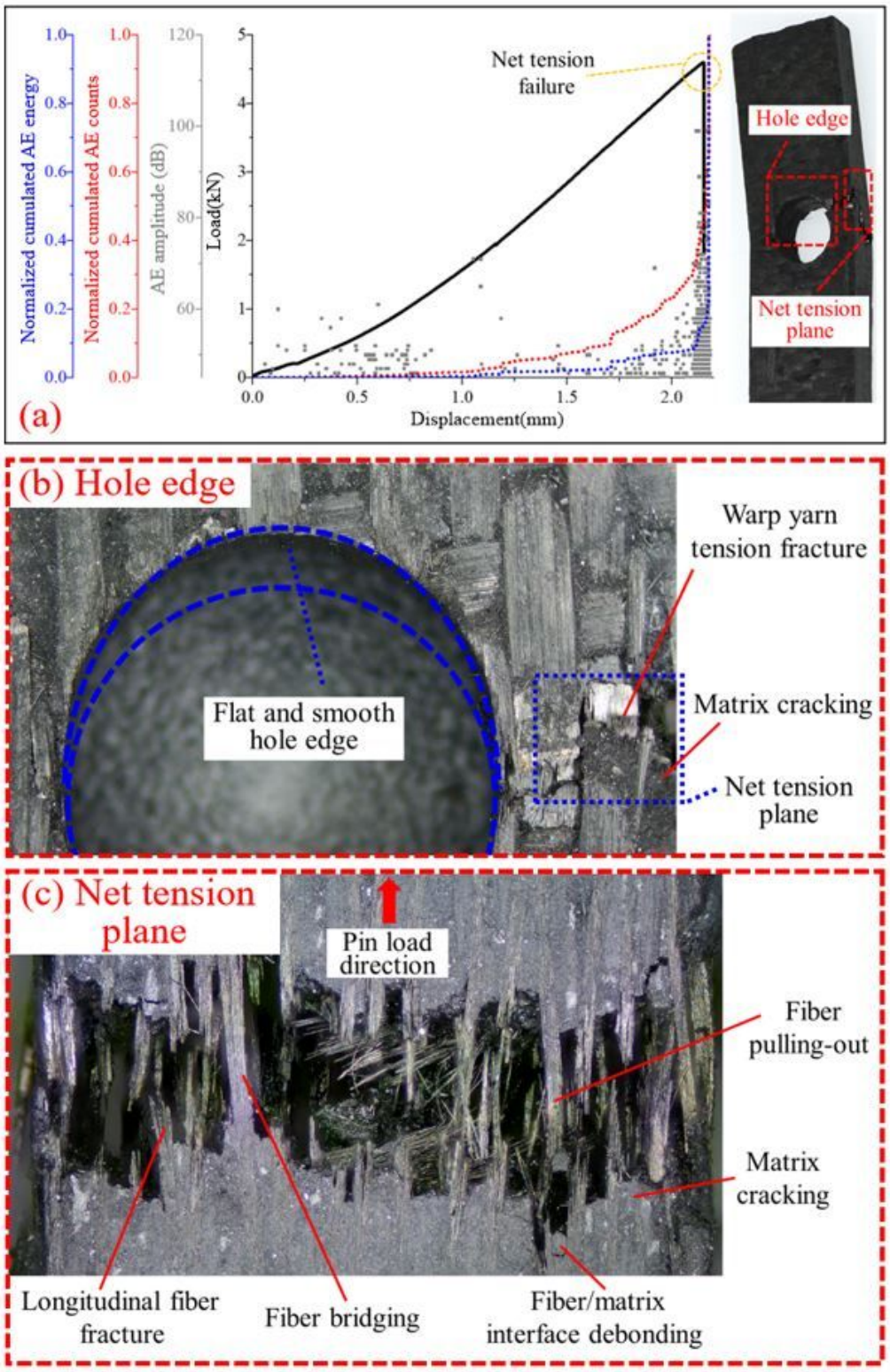

Figure 6

(a) Load and AE events vs. displacement curves and (b) morphology of the hole edge and (c) net tension plane for type A.

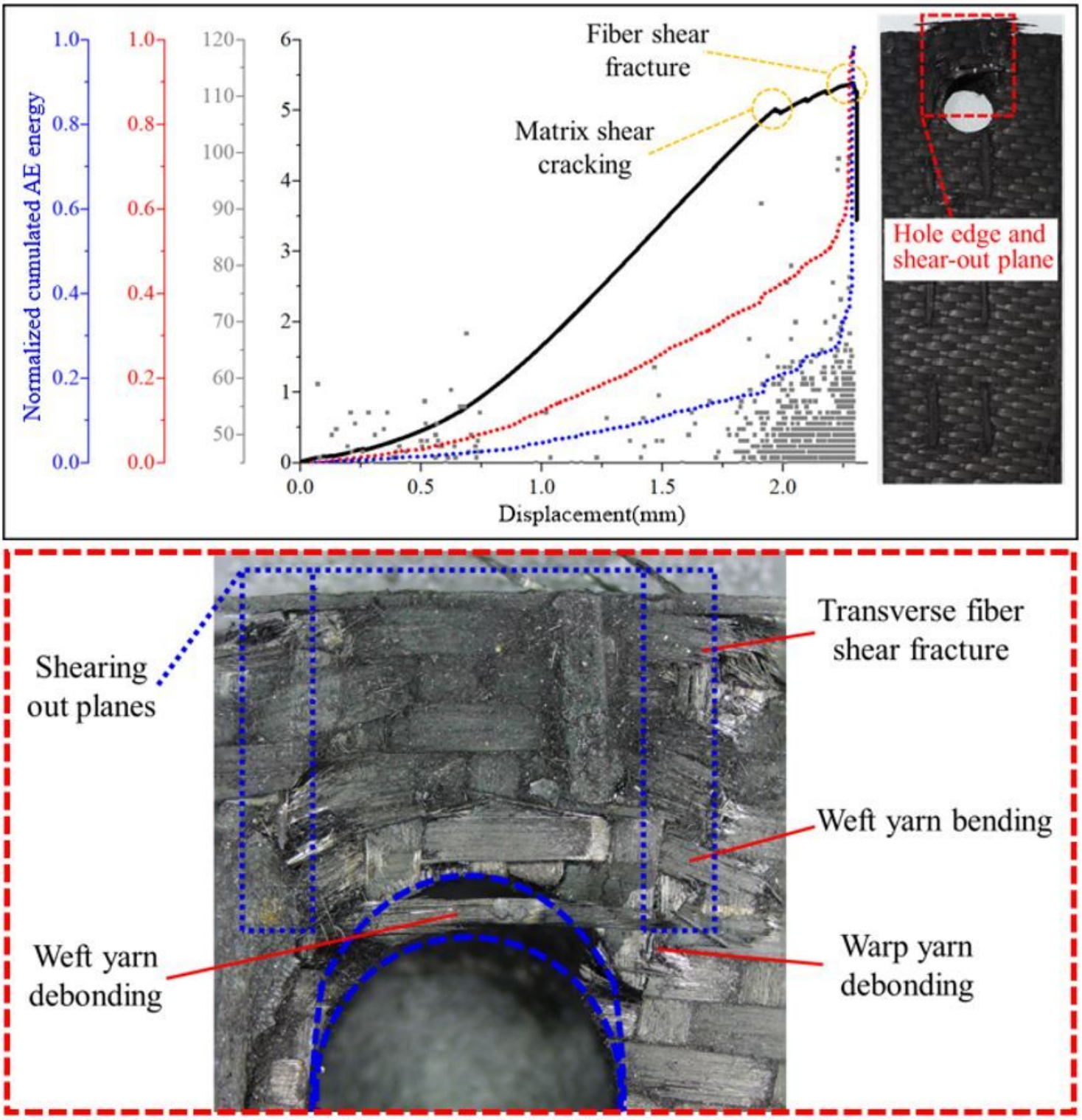

Figure 7

Load and AE events vs. displacement curves and morphology of the hole edge and shear-out plane for type D.

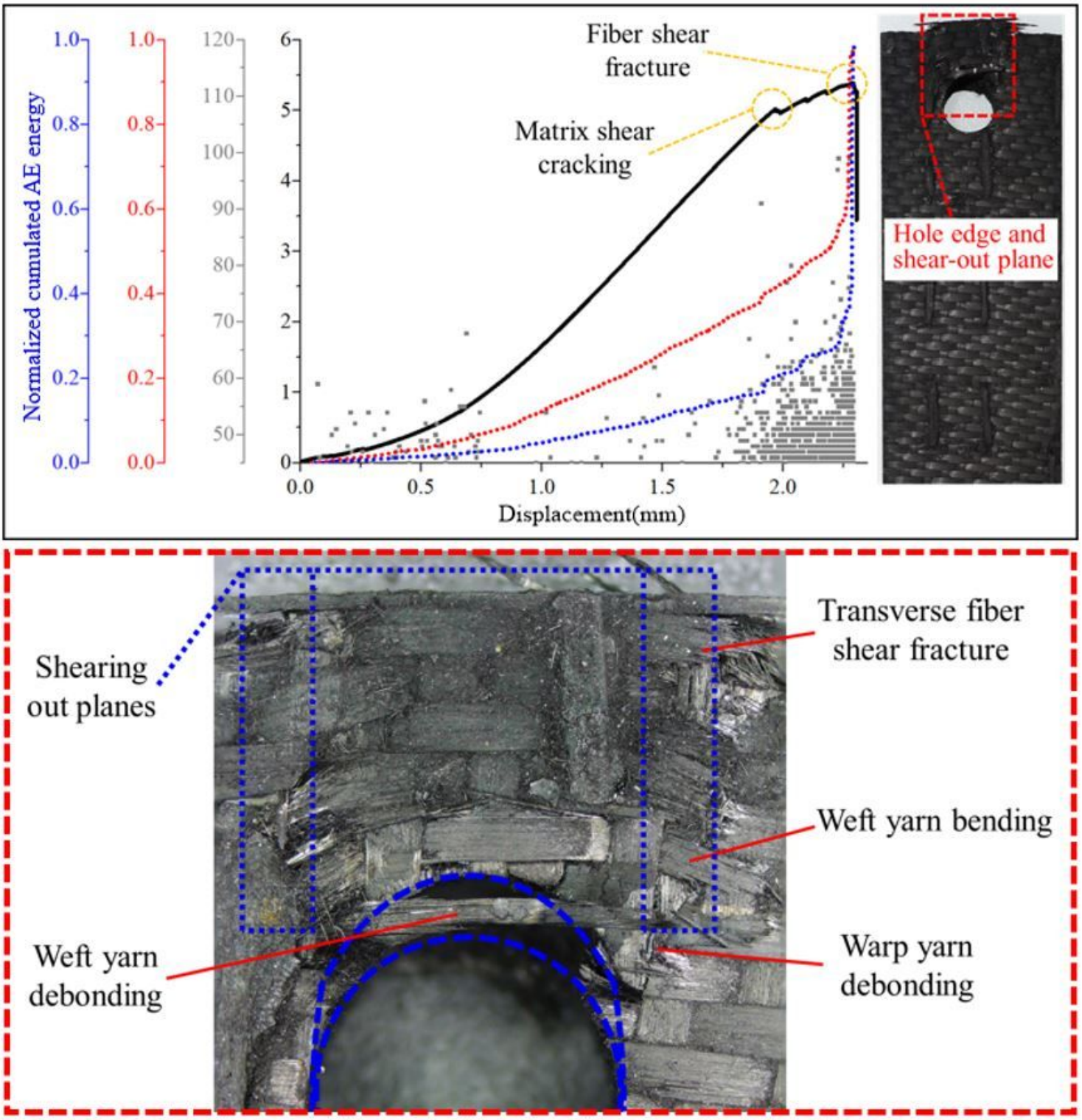

Figure 7

Load and AE events vs. displacement curves and morphology of the hole edge and shear-out plane for type D.

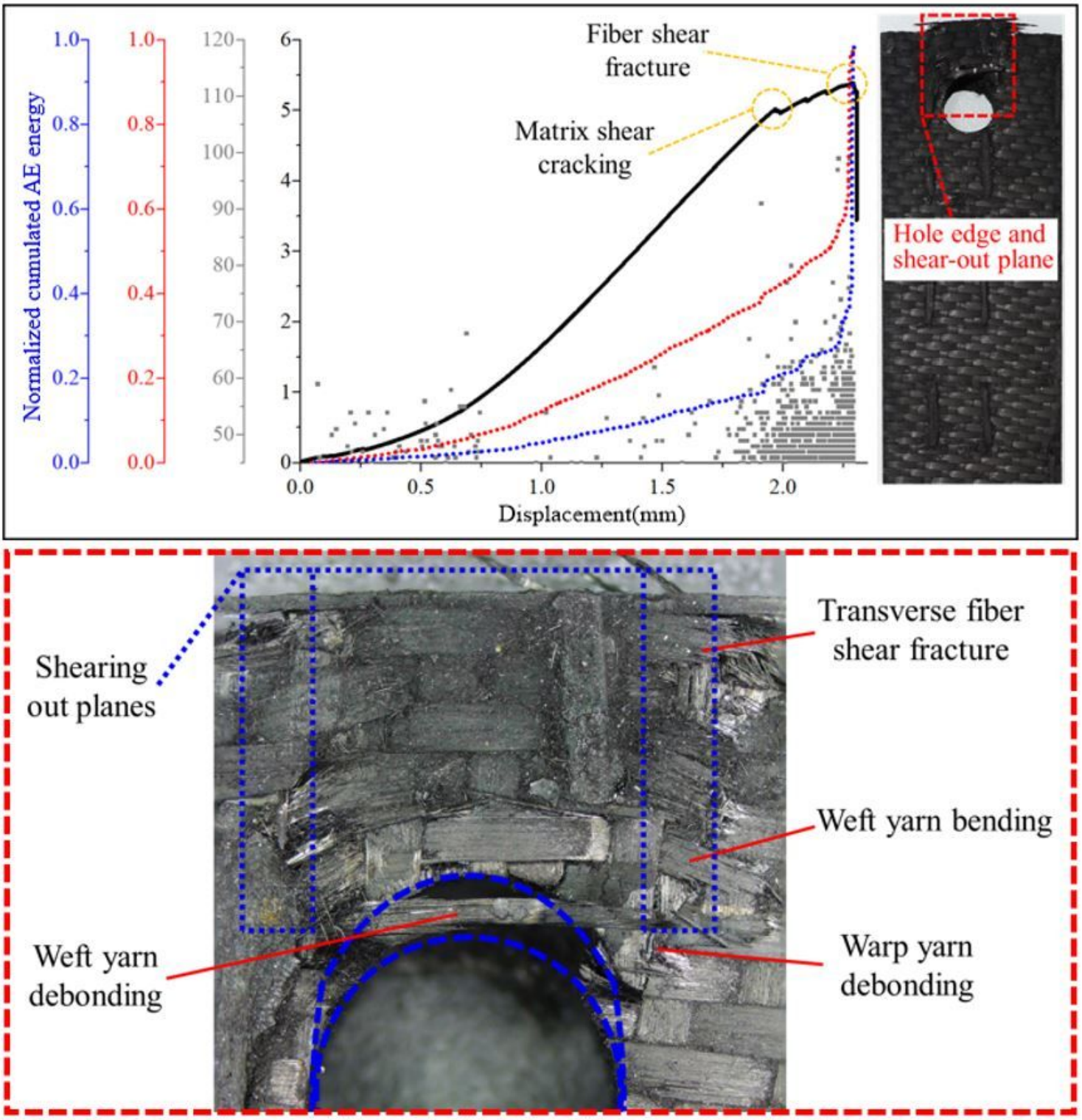

Figure 7

Load and AE events vs. displacement curves and morphology of the hole edge and shear-out plane for type D.

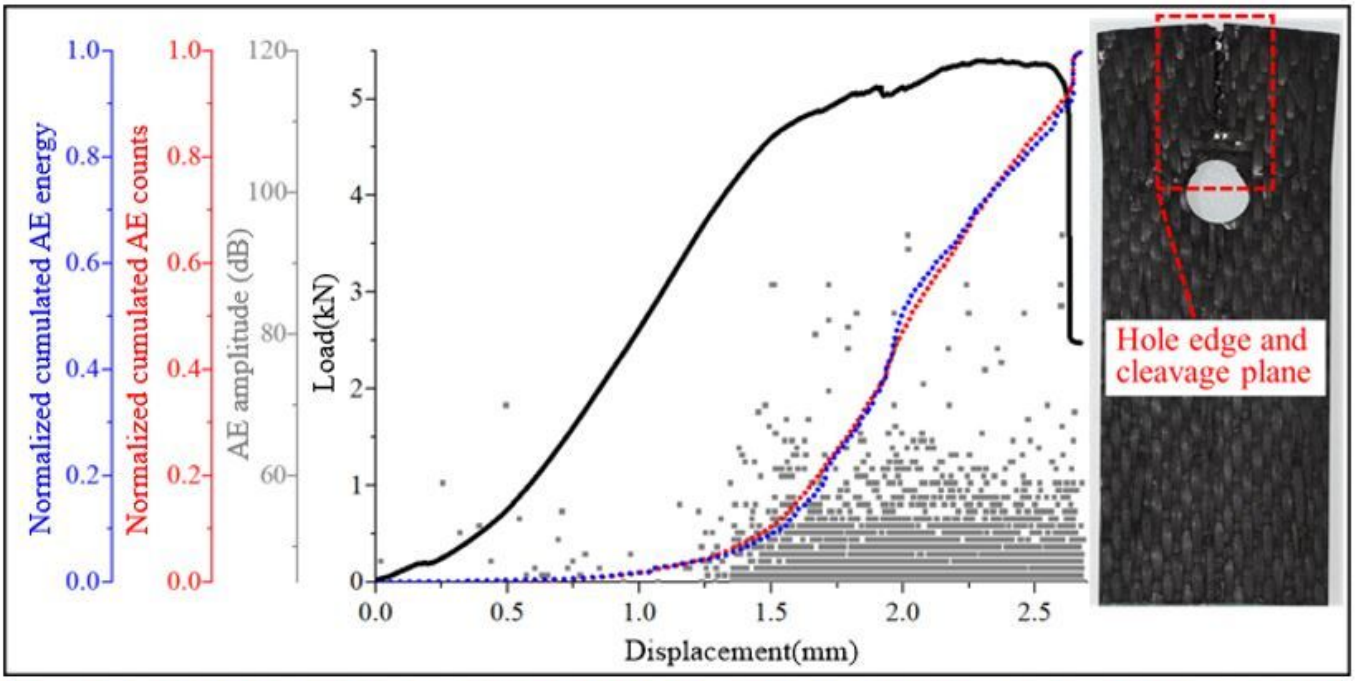

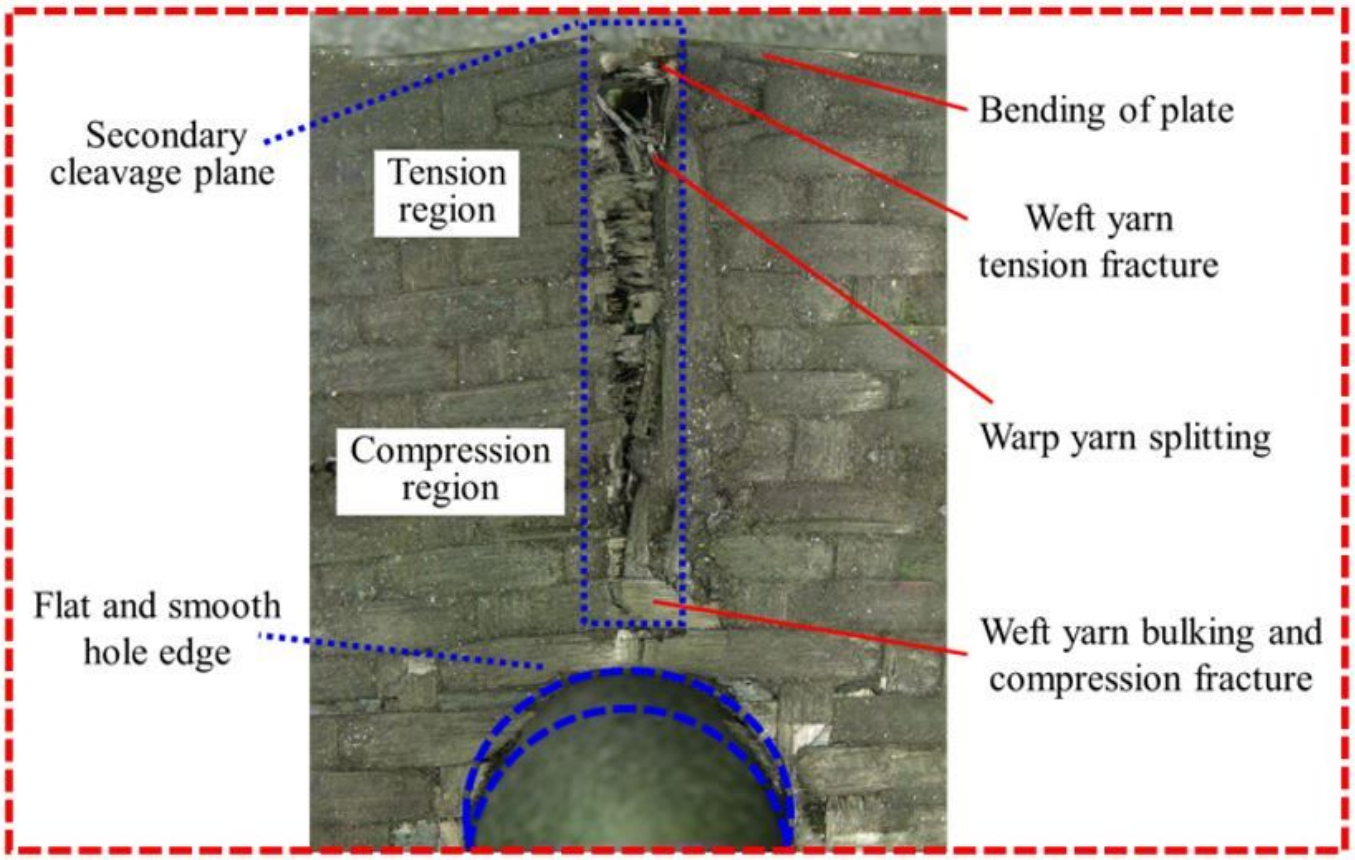

Figure 8

Load and AE events vs. displacement curves and morphology of the hole edge and cleavage plane for type E.

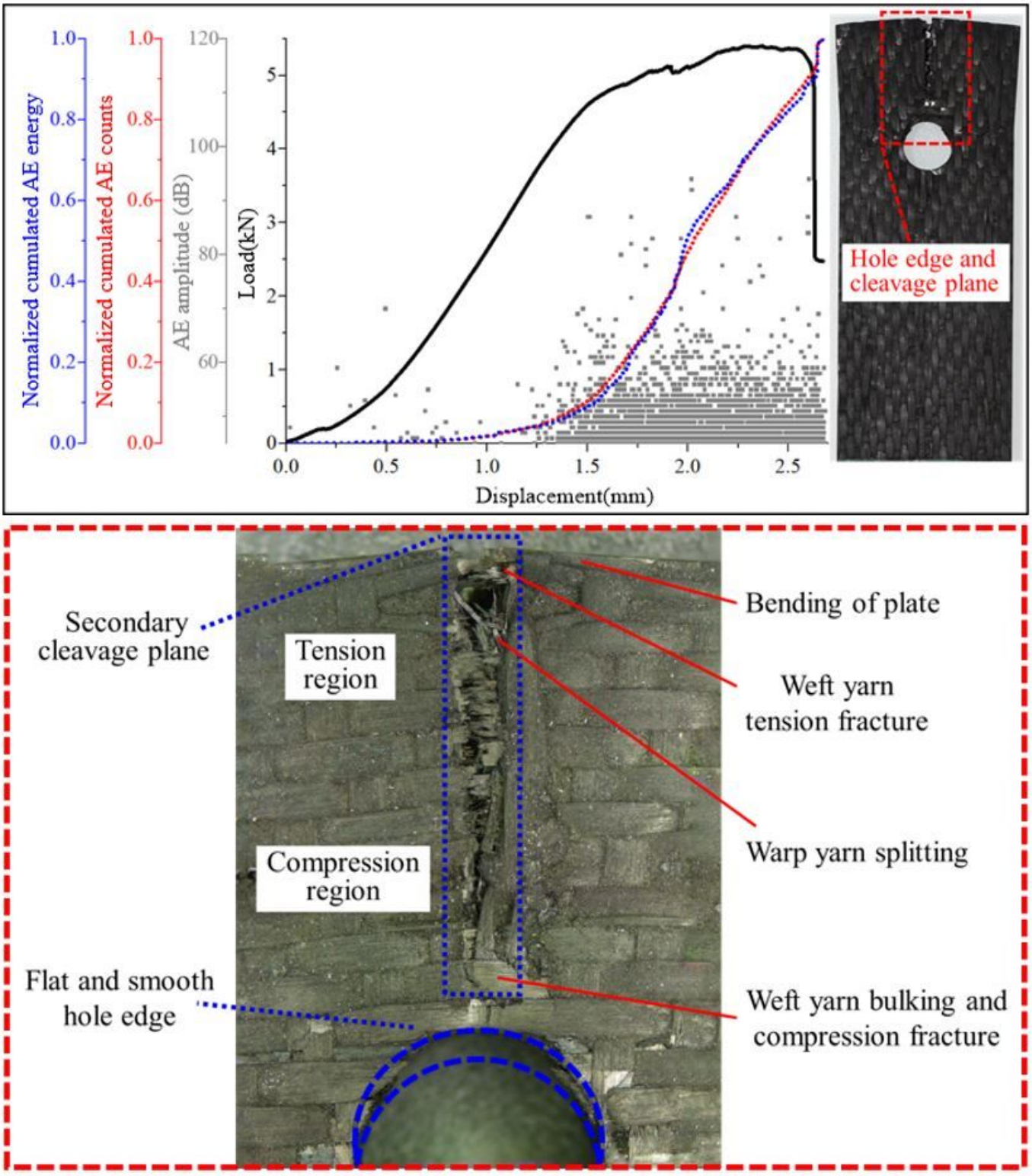

Figure 8

Load and AE events vs. displacement curves and morphology of the hole edge and cleavage plane for type E.

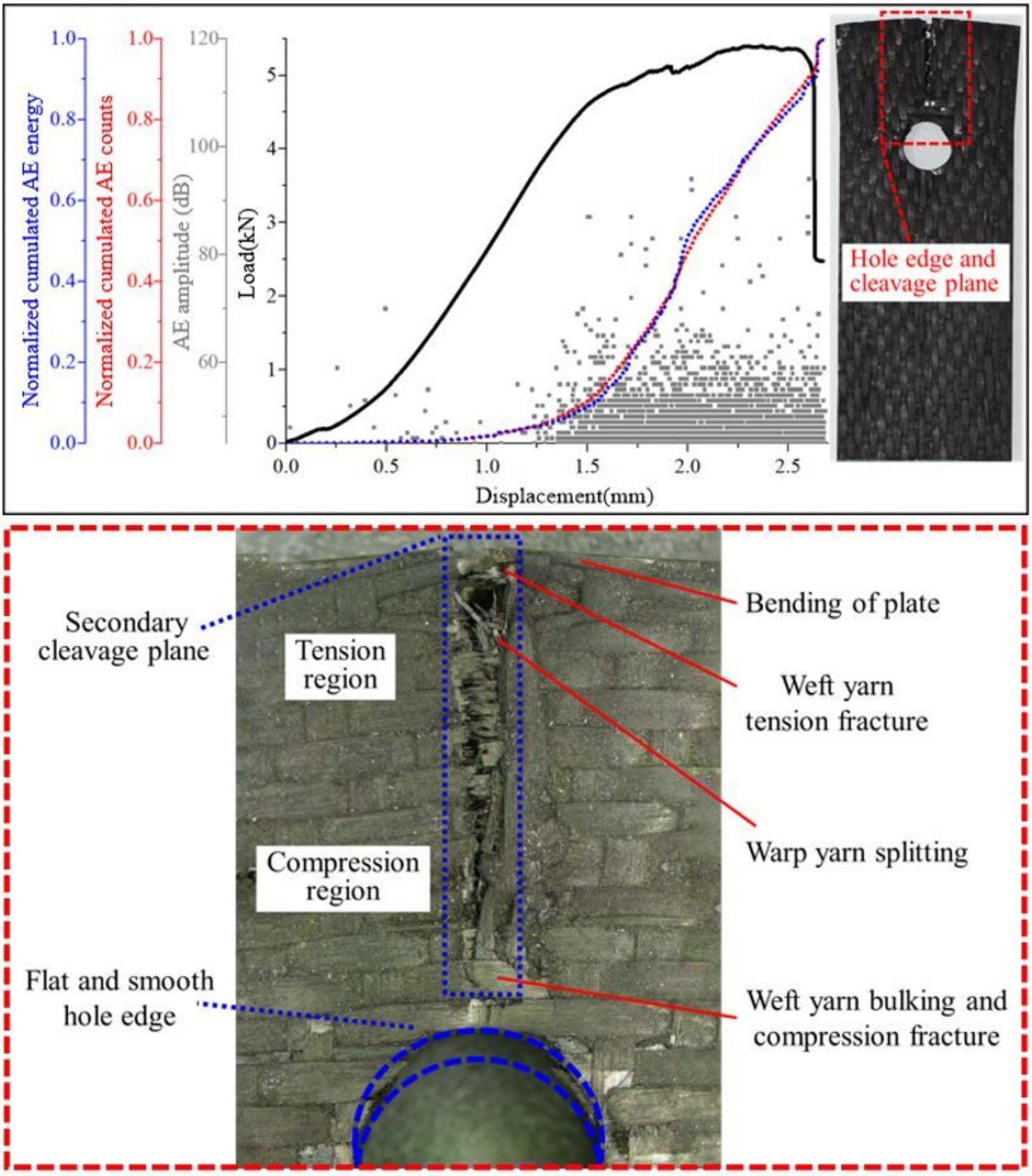

Figure 8

Load and AE events vs. displacement curves and morphology of the hole edge and cleavage plane for type E.

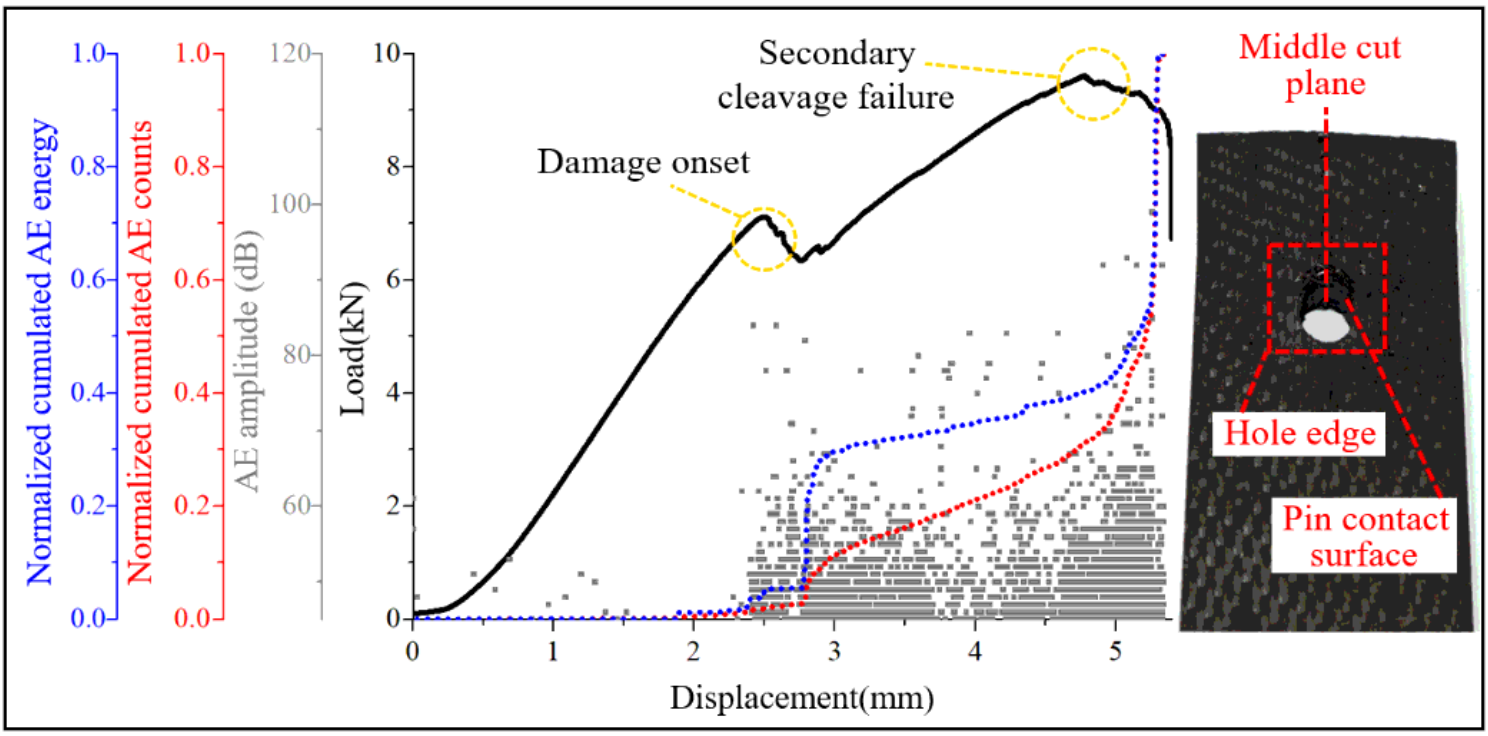

Figure 9

Load and AE events vs. displacement curves for type C.

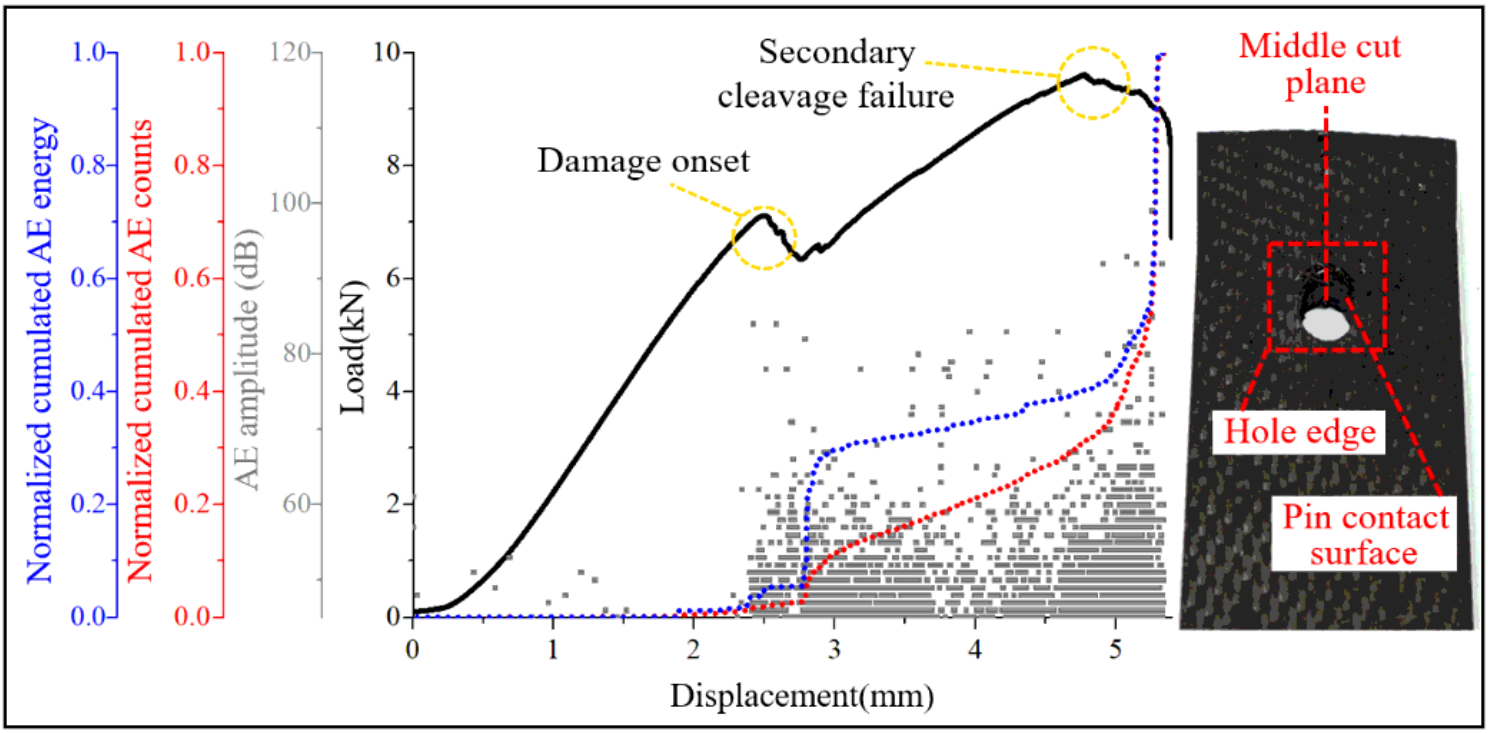

Figure 9

Load and AE events vs. displacement curves for type C.

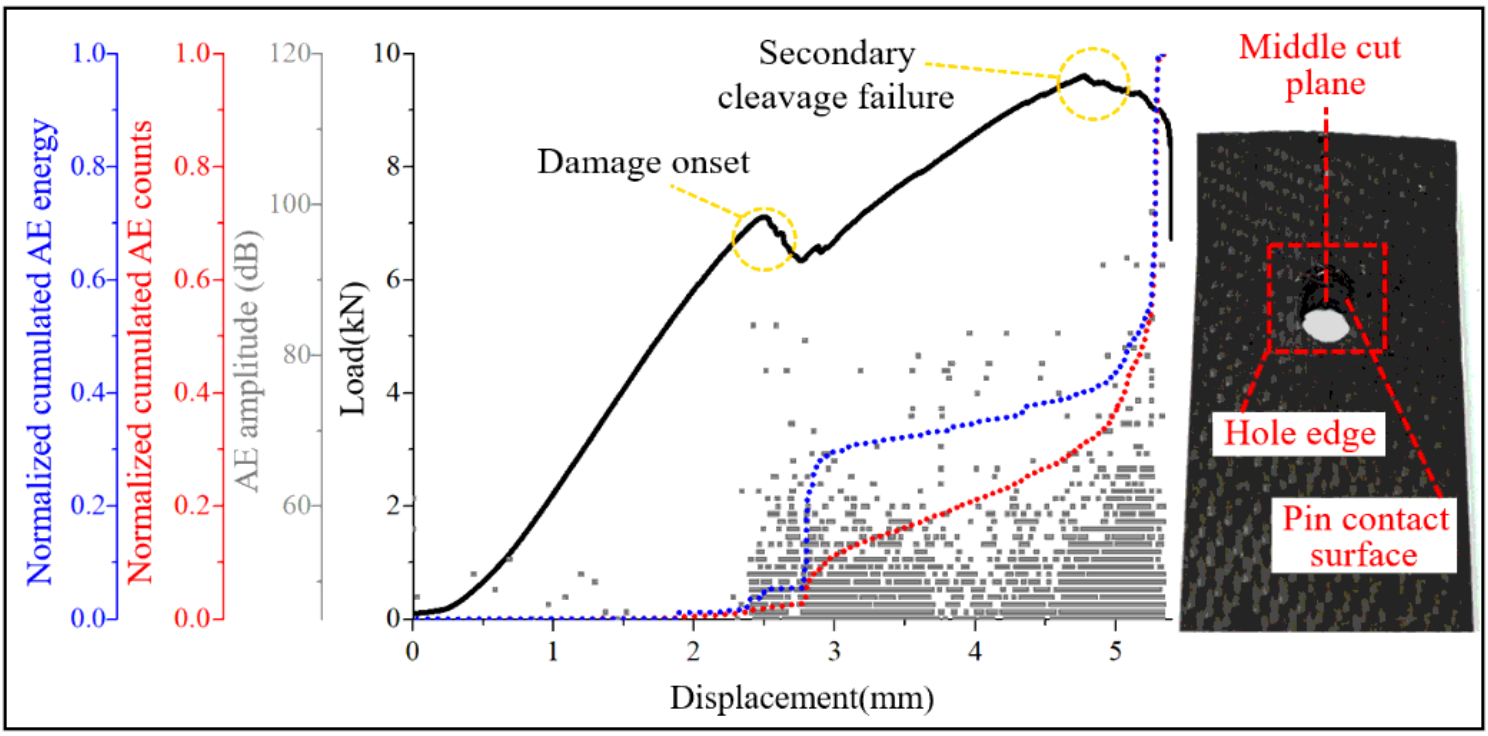

Figure 9

Load and AE events vs. displacement curves for type C.

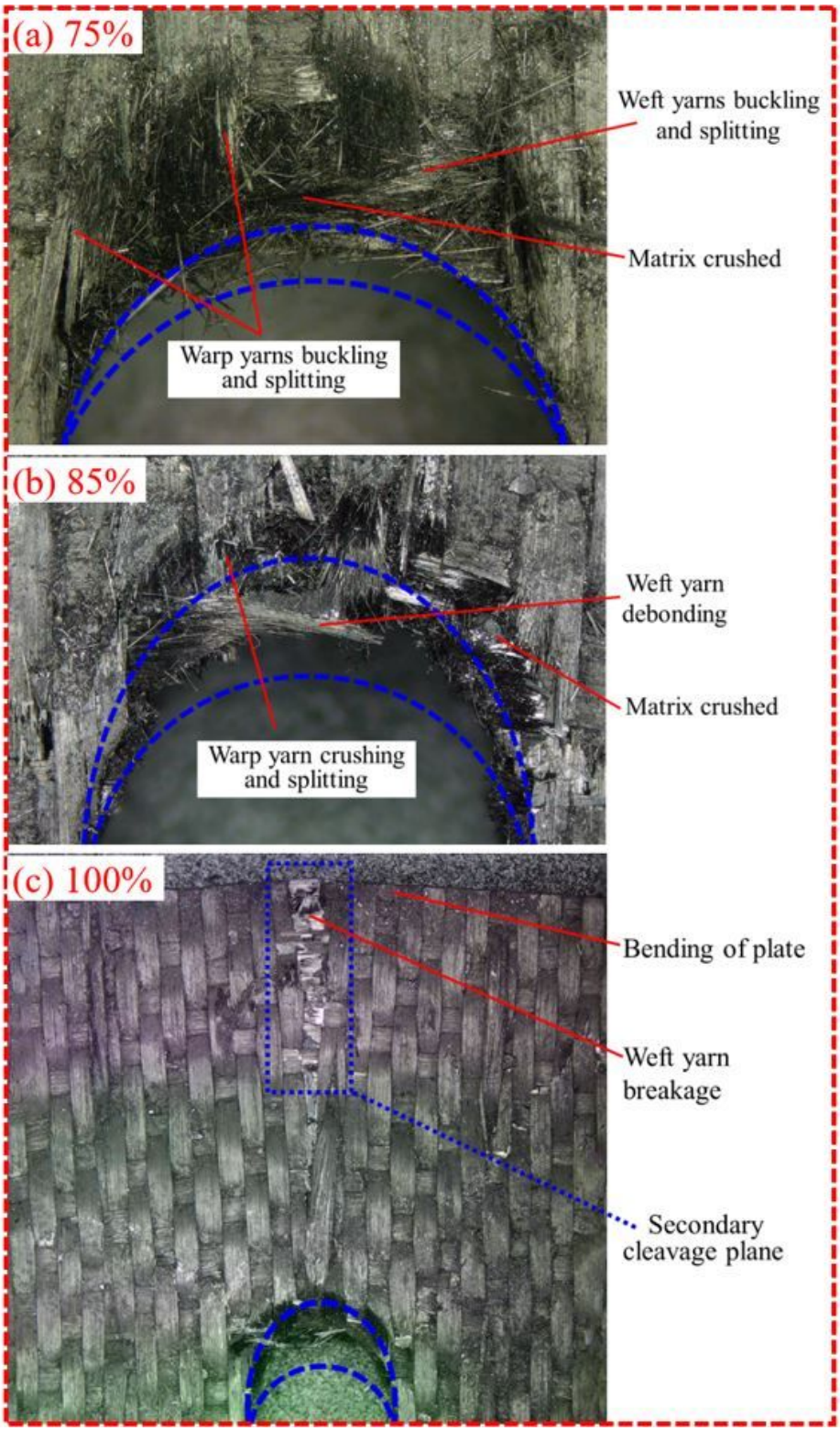

Figure 10

Morphology of the hole edge for type C at the level of (a) 75%, (b) 85% and (c) 100% of the maximum load.

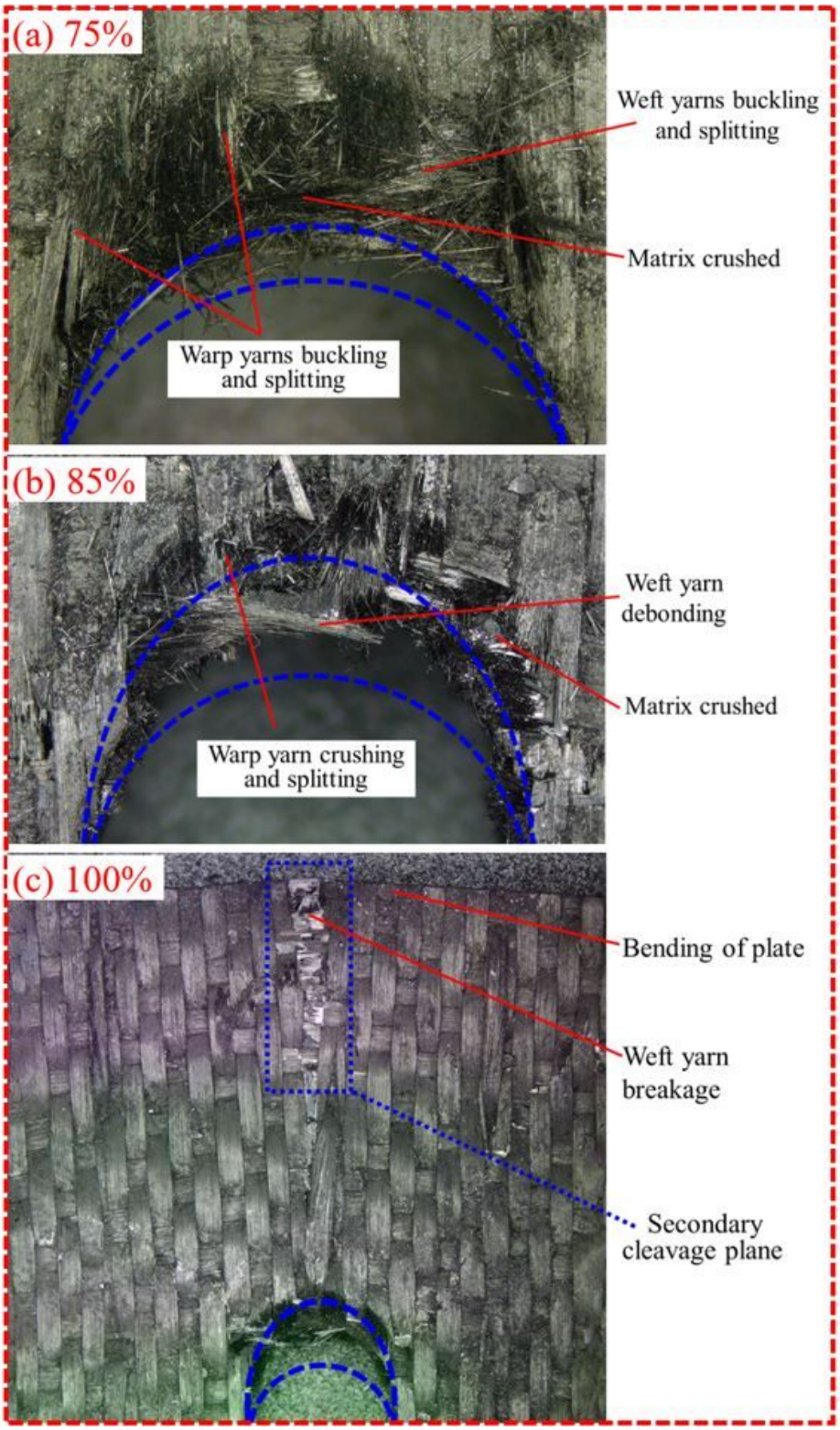

Figure 10

Morphology of the hole edge for type C at the level of (a) 75%, (b) 85% and (c) 100% of the maximum load.

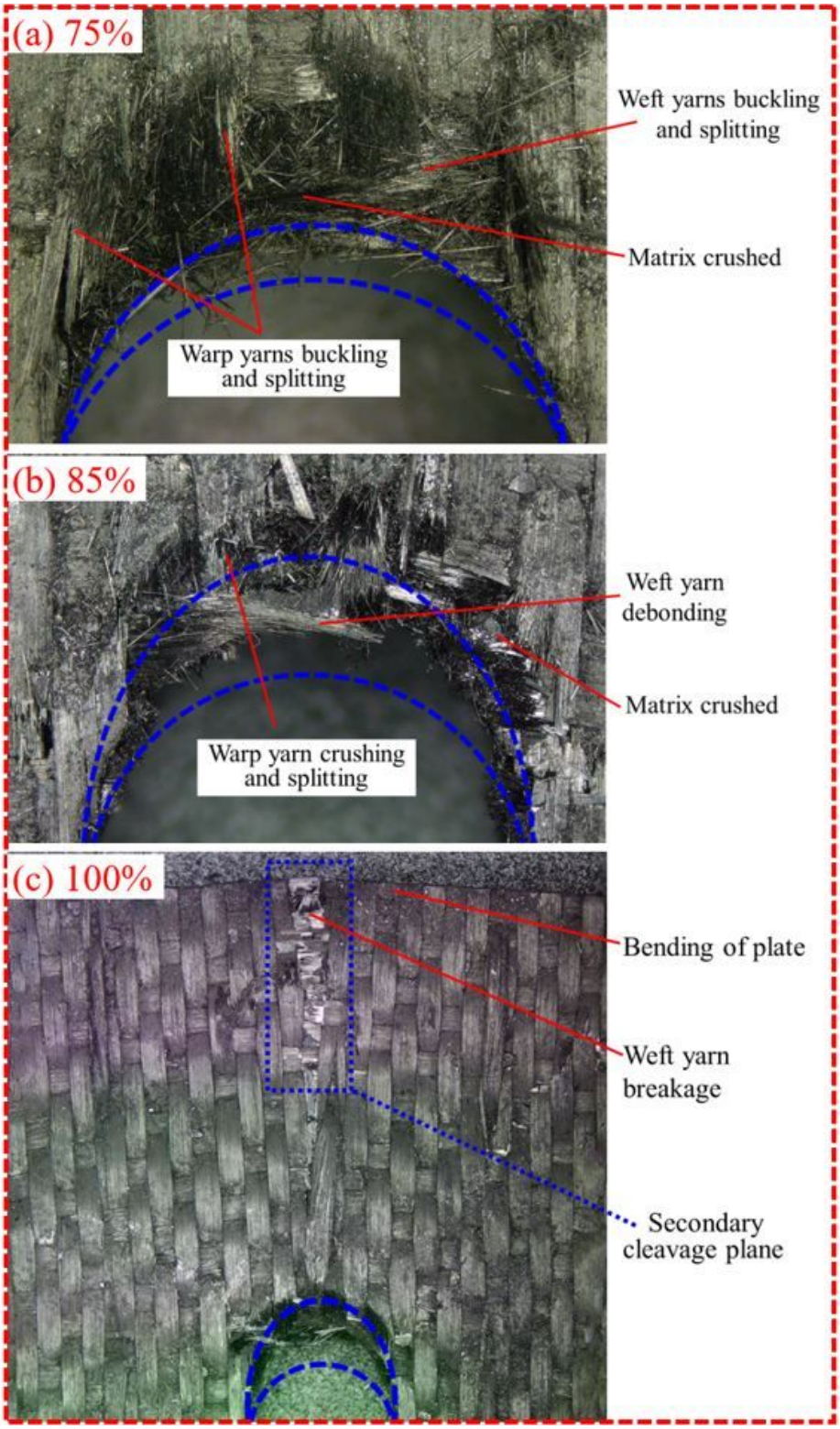

Figure 10

Morphology of the hole edge for type C at the level of (a) 75%, (b) 85% and (c) 100% of the maximum load.

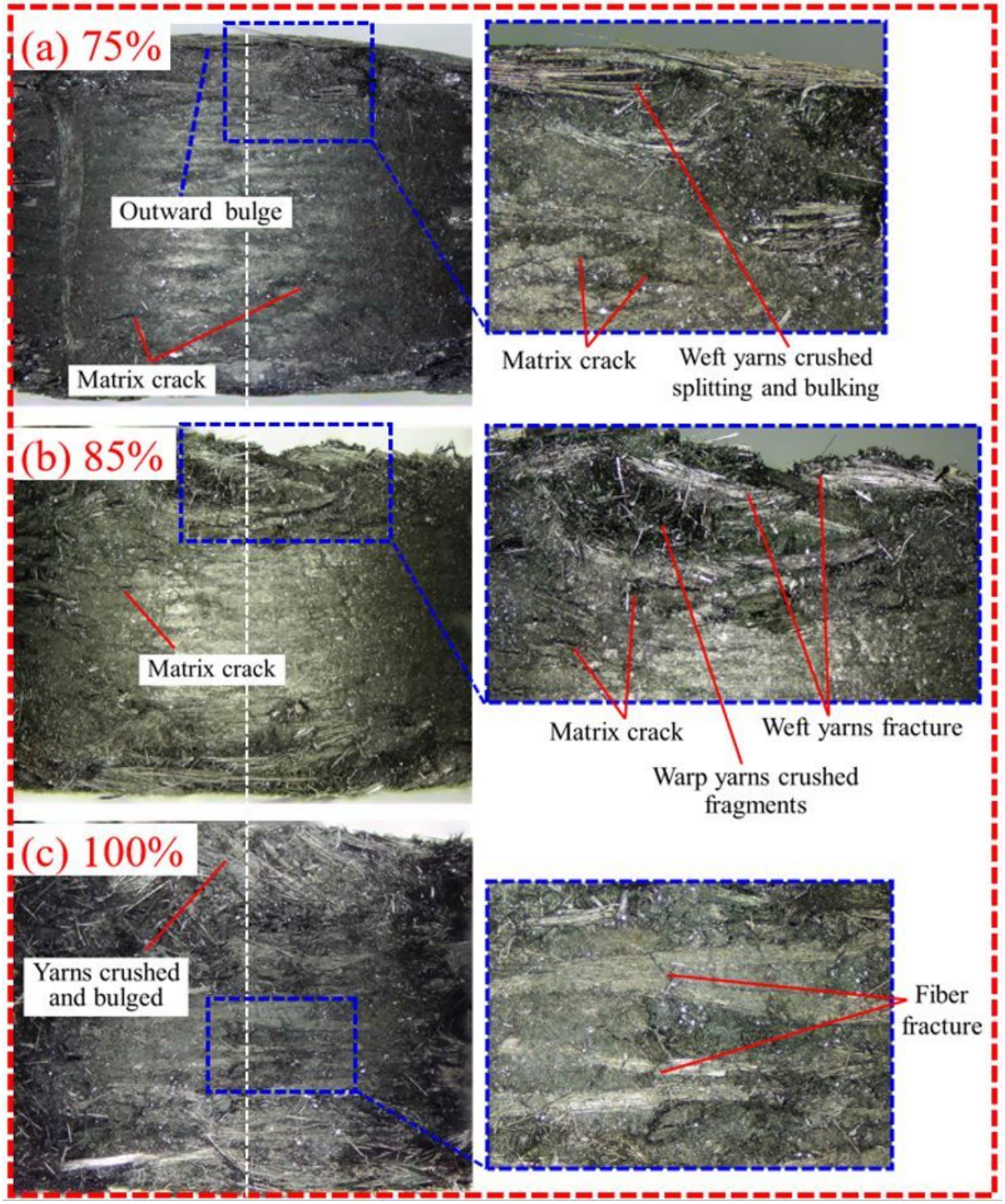

Figure 11

Morphology of the pin contact surface for type C at the level of (a) 75%, (b) 85% and (c) 100% of the maximum load.

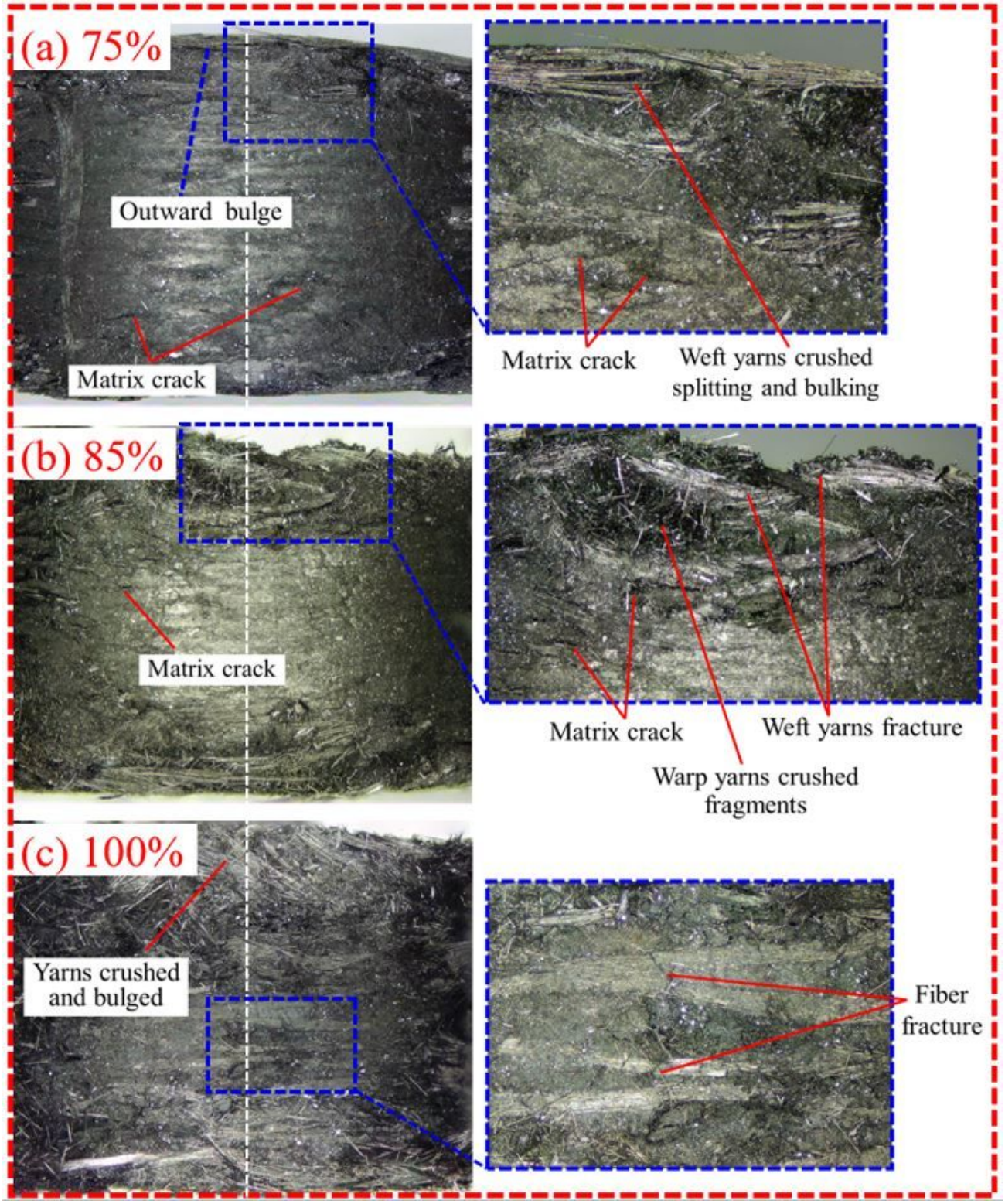

Figure 11

Morphology of the pin contact surface for type C at the level of (a) 75%, (b) 85% and (c) 100% of the maximum load.

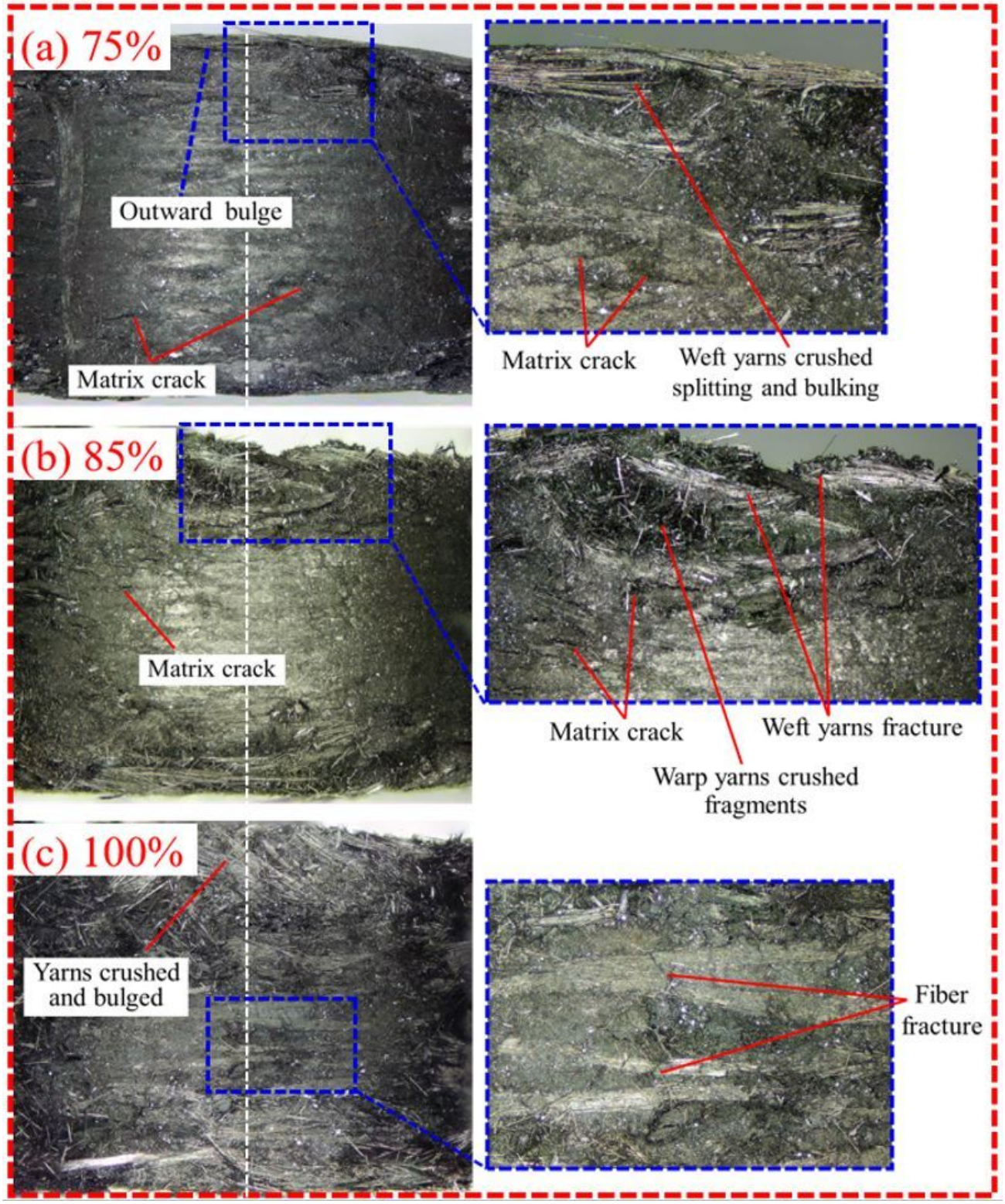

Figure 11

Morphology of the pin contact surface for type C at the level of (a) 75%, (b) 85% and (c) 100% of the maximum load.

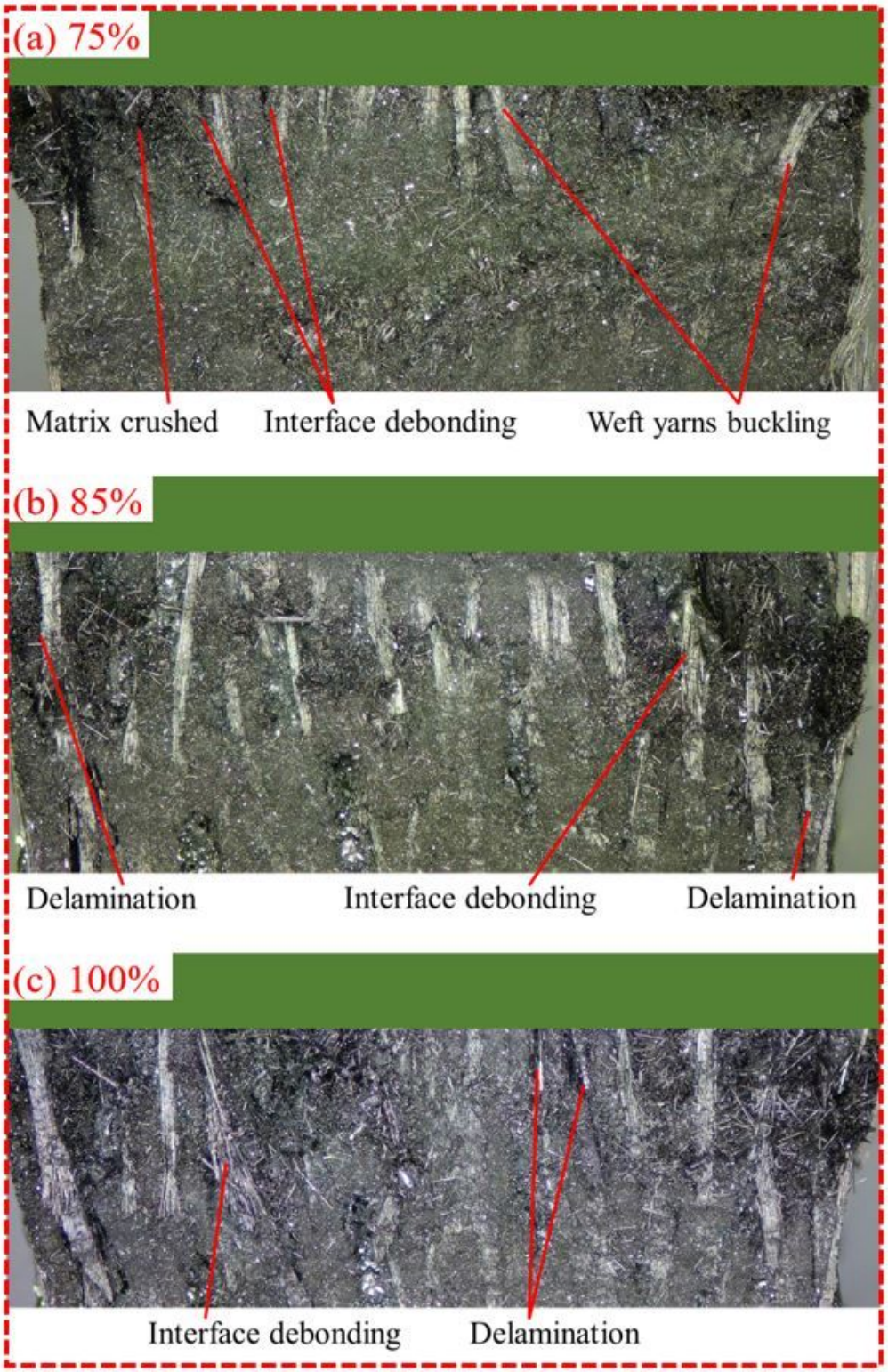

Figure 12

Morphology of the middle cut plane for type C at the level of (a) 75%, (b) 85% and (c) 100% of the maximum load.

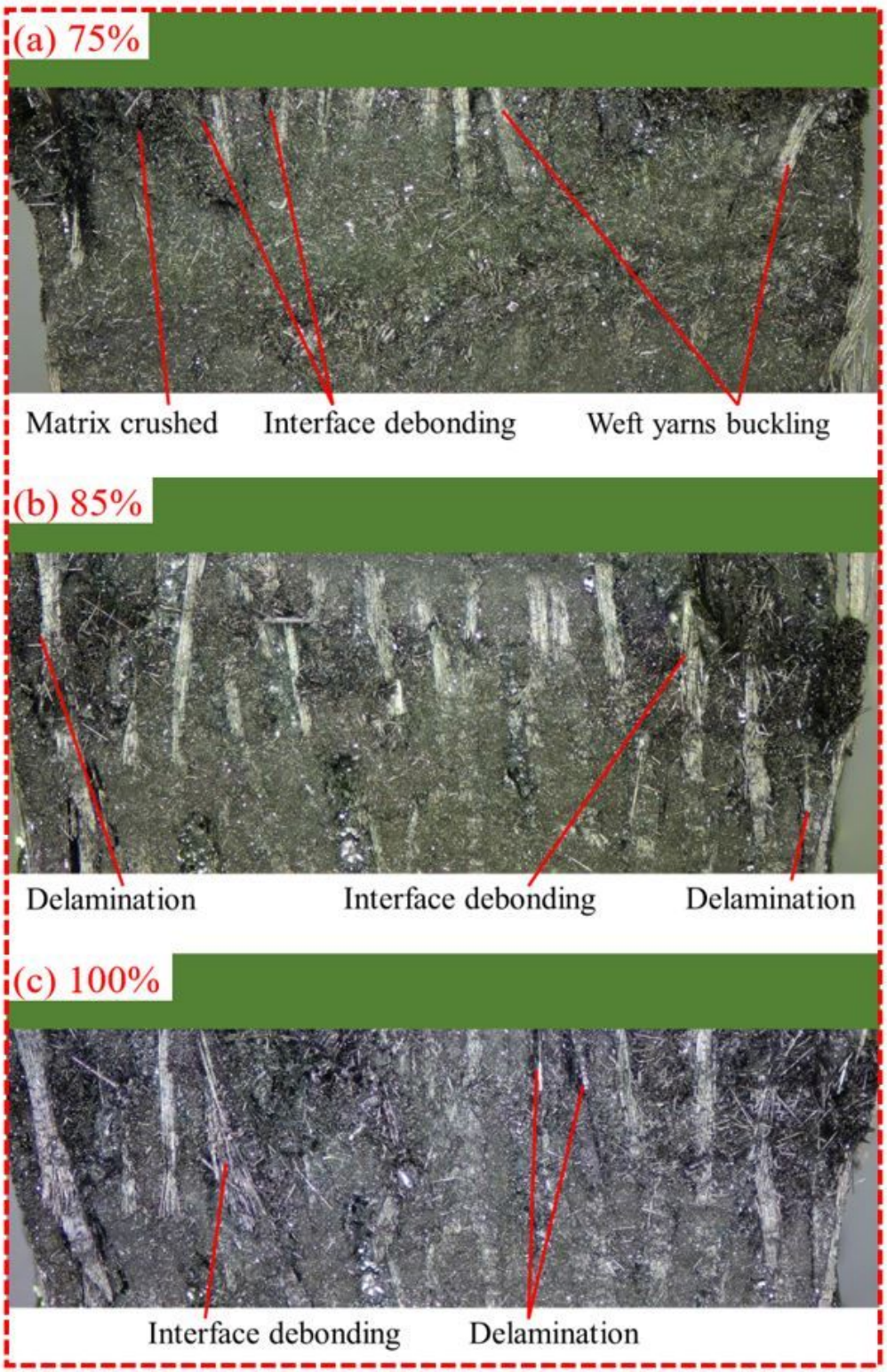

Figure 12

Morphology of the middle cut plane for type C at the level of (a) 75%, (b) 85% and (c) 100% of the maximum load.

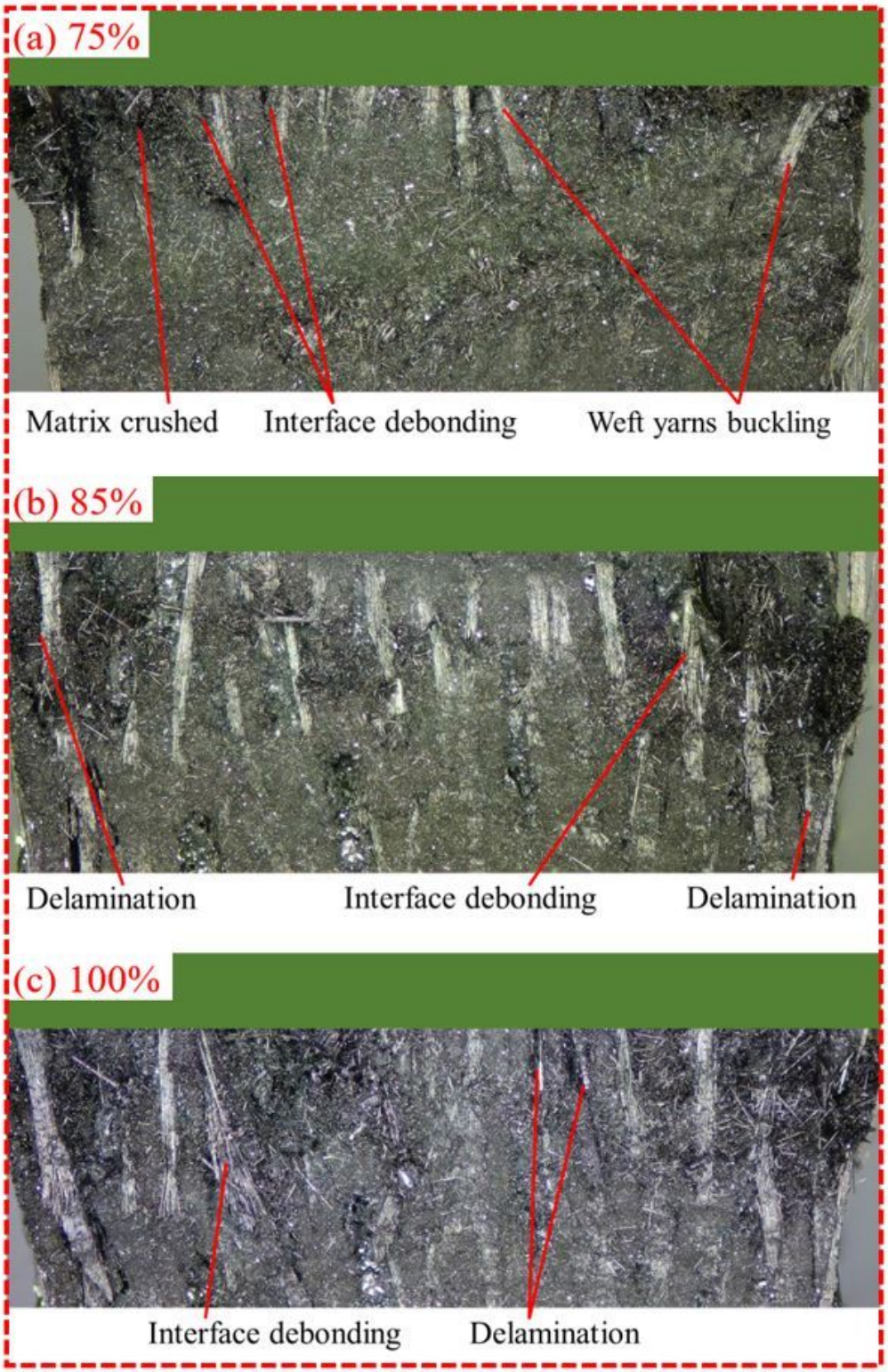

Figure 12

Morphology of the middle cut plane for type C at the level of (a) 75%, (b) 85% and (c) 100% of the maximum load.

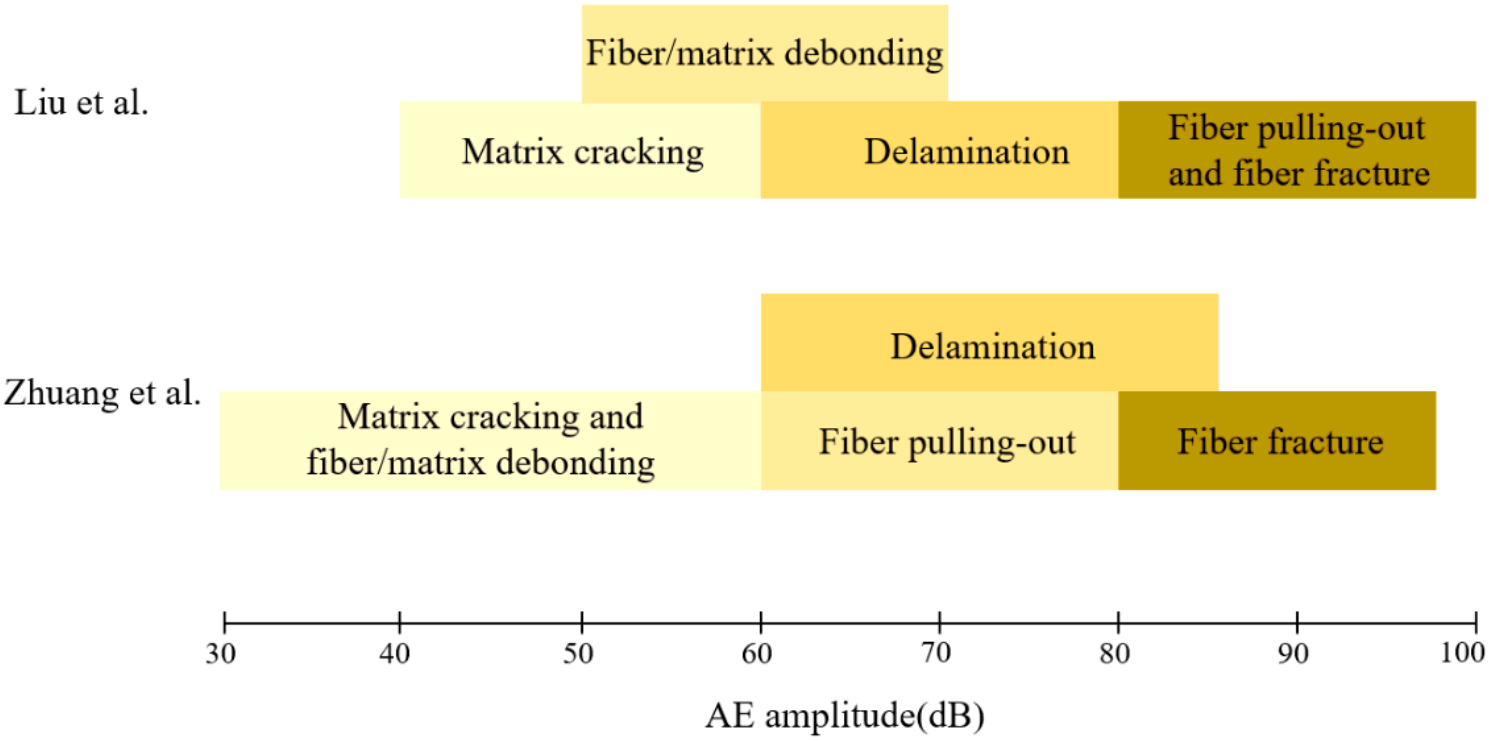

Figure 13

The amplitude ranges defined in Liu et al. [22] and Zhuang et al. [23].

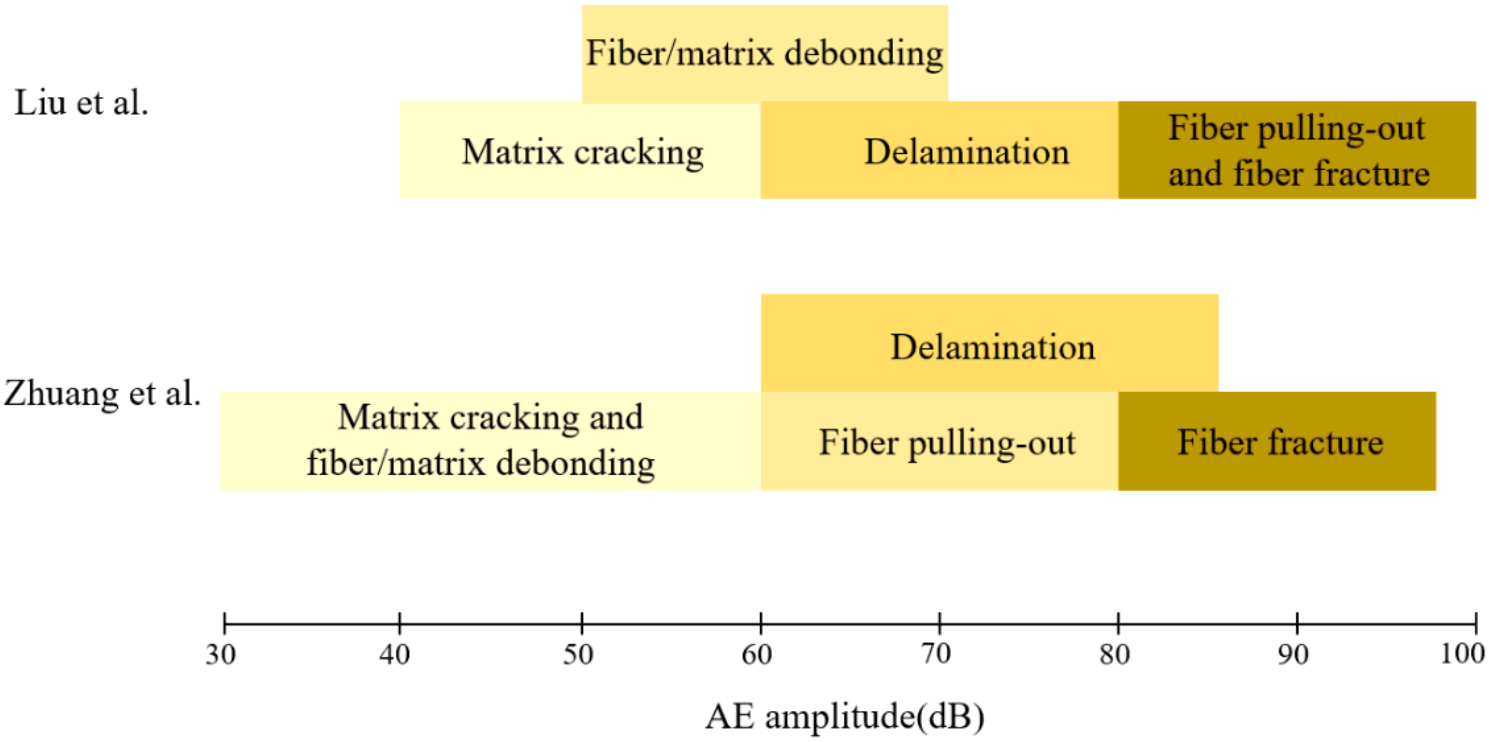

Figure 13

The amplitude ranges defined in Liu et al. [22] and Zhuang et al. [23].

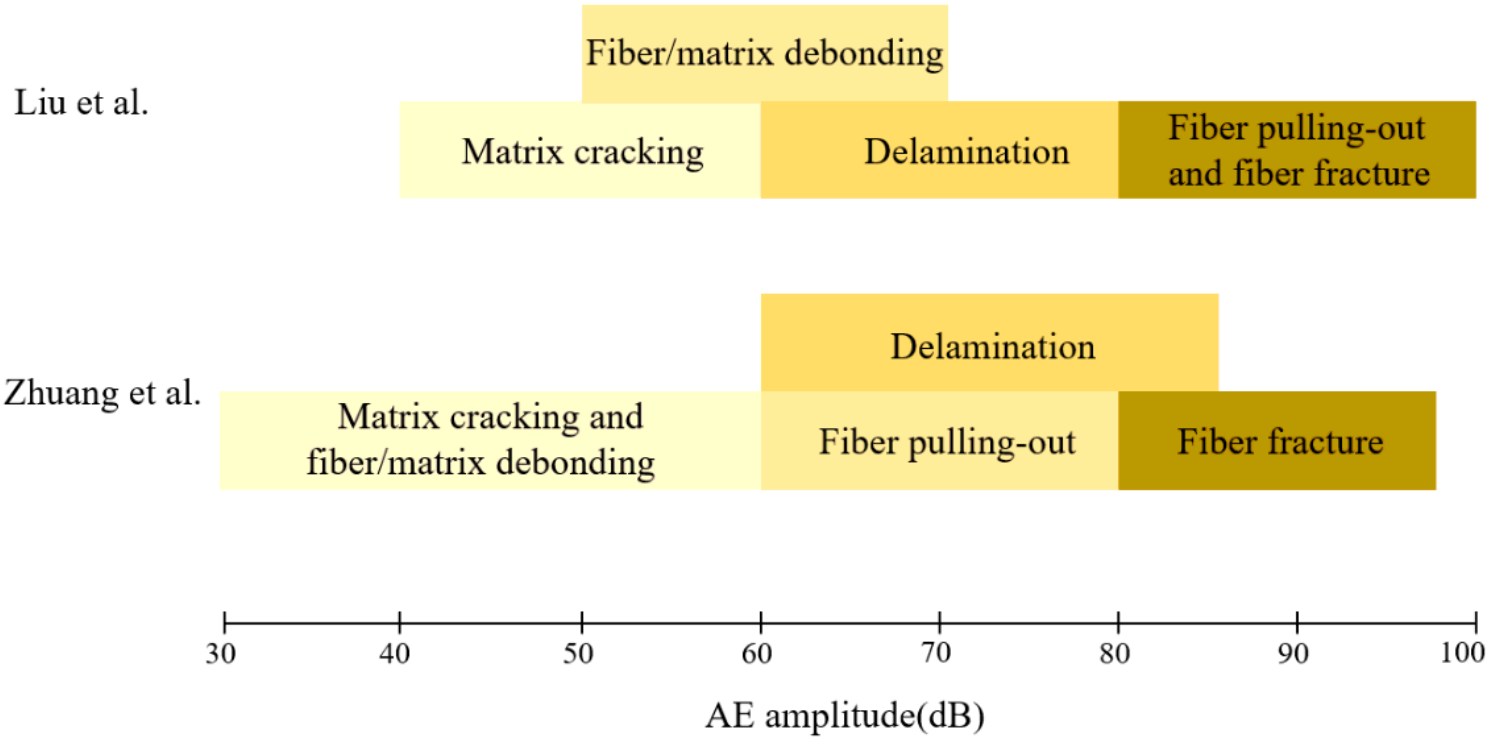

Figure 13

The amplitude ranges defined in Liu et al. [22] and Zhuang et al. [23].